Multiphase phenomena in Diesel fuel injection systems

Ioannis K. Karathanassis[a,1], *Foivos Koukouvinis*[b,1], *Manolis Gavaises*[c,1]

1. City, University of London, School of Mathematics, Computer Science & Engineering, Northampton Square, London EC1V 0HB, UK

Email: (a) ioannis.karathanassis@city.ac.uk,
(b) foivos.koukouvinis.1@city.ac.uk,
(c) m.gavaises@city.ac.uk

Introduction

Fuel Injection Equipment (FIE) are an integral component of modern Internal Combustion Engines (ICE), since they play a crucial role in the fuel atomization process and in the formation of a fuel/air combustible mixture, consequently affecting efficiency and pollutant formation. Advancements and improvements of FIE systems are determined by the complexity of the physical mechanisms taking place; the spatial scales are in the order of millimetres, flow may become locally highly supersonic, leading to very small temporal scales of microseconds or less. The operation of these devices is highly unsteady, involving moving geometries such as needle valves. Additionally, extreme pressure changes imply that many assumptions of traditional fluid mechanics, such as incompressibility, are no longer valid. Furthermore, the description of the fuel properties becomes an issue, since fuel databases are scarce or limited to pure components, whereas actual fuels are commonly hydrocarbon mixtures. Last but not least, complicated phenomena such as phase change or transition from subcritical to transcritical/supercritical state of matter further pose complications in the understanding of the operation of these devices.

The link between nozzle flow and spray formation has long been an open issue in the IC engines community. Phase-change dominates injection of liquid fuels into combustion engines. Depending on the nozzle design and/or operating conditions, cavitation or flash boiling (for gasoline injectors) are the first phase-change processes taking place even before reaching the combustion chamber and affect atomisation. It is widely accepted that nozzle flow plays a major role in fuel atomisation and emissions in Diesels. Today's commercial FIE reach 2750bar while injection pressures as high as 4,500bar are being investigated. The present work aims to discuss in detail the importance of phase change phenomena and flow mechanisms in the operation of FIE equipment, or simplified models resembling such equipment, discussing internal flow effects. Also, a brief discussion on fuel properties, subcritical/transcritical fluid state and how it affects atomization will be discussed. The discussions will be based on prior experimental investigations or numerical studies of the authors' group.

Flow topology

Real-size exact replicas of Diesel nozzles made from transparent (e.g. acrylic) materials have been successfully manufactured, able to withstand pressures of the order of 1000 bar[1]. Parallel to those activities, several studies have focused on illustrating the in-nozzle, two-phase flow topology in transparent, enlarged replicas at lower injection pressures (see selectively [2–4]). Flow similarity to the actual injector flow is ensured based on non-dimensional numbers, i.e. with the use of the Reynolds and cavitation numbers defined as follows:

$$Re = \frac{u \cdot D}{\nu} \tag{1}$$

$$CN = \frac{p_{inj} - p_o}{p_o - p_{sat}} \quad (2)$$

where u, D and v in the Reynolds-number definition are the flow average velocity, the orifice internal diameter and the diesel kinematic viscosity, respectively. Referring to the cavitation number definition, p_{inj}, p_o and p_{sat} are the injection, back (outlet) and saturation pressure, respectively. An additional definition of the cavitation number has also been used in the literature[5]:

$$\sigma = \frac{p_{inj} - p_{sat}}{\frac{1}{2}\rho u^2} \quad (3)$$

where ρ, u are the fuel density and the flow velocity, respectively. Nevertheless, Equation (2) will be used throughout this chapter where increasing values of CN correspond to more extensive cavitation formation.

Optical methods

Optical methods, i.e. back-light diffuse illumination or Mie scattering,[6–8] have been extensively employed for the visualization of cavitating structures emerging in injector flows. Such methods benefit from a relatively simple and straightforward optical set-up, mainly comprising an illumination source, a set of diffusers/lenses and a high-speed camera recording either the shadows or the Mie signal produced by the vapour formed within the injector orifice. The schematic shown in Figure 1 illustrates the assembly of a real-size injector with a transparent tip. The metallic body of the actual injector is machined-off below the sac region and an acrylic part realising the sac and injector holes is clamped into position (Figure 1a), allowing the internal flow to be realised from different angles (Figure 1b). Due to the limited durability of acrylic, experiments reported in this chapter have been performed for injection pressures up to 500 bars[9].

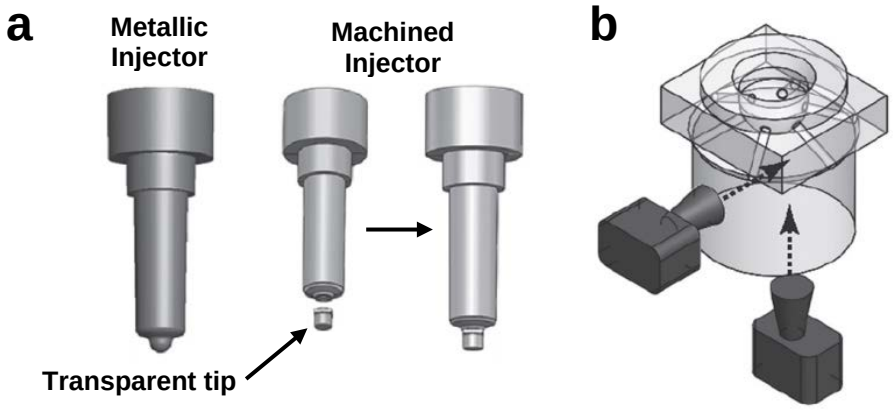

Figure 1. (a) Nominal fabrication steps of injector/transparent tip assembly (b) 3-D view of the transparent-tip schematic indicating visualisation angles. The tip realises a six-hole Diesel injector, with all holes at angles of 65^o with reference to the injector main axis[9].

A representative injection event employing the transparent tip depicted in Figure 1 is presented in Figure 2, illustrating the formation of cavitation in the sac region and injector holes. The sequence at 0 ms reveals that bubbles, consisting of congested gas and/or fuel vapour, occupy a large portion of the sac and injector-hole regions prior to injection. Latter time instances clearly demonstrate the presence of fuel vapour clouds within the injector hole during the needle-opening phase. As can be seen, cavitation is always evident during the first half of injection duration with the cavity forming in the sac region, in the vicinity of the needle tip and propagating into the orifice core. These distinct cavitation structures of elongated shape, which are not attached to the injector walls, are characteristically termed as string cavities.

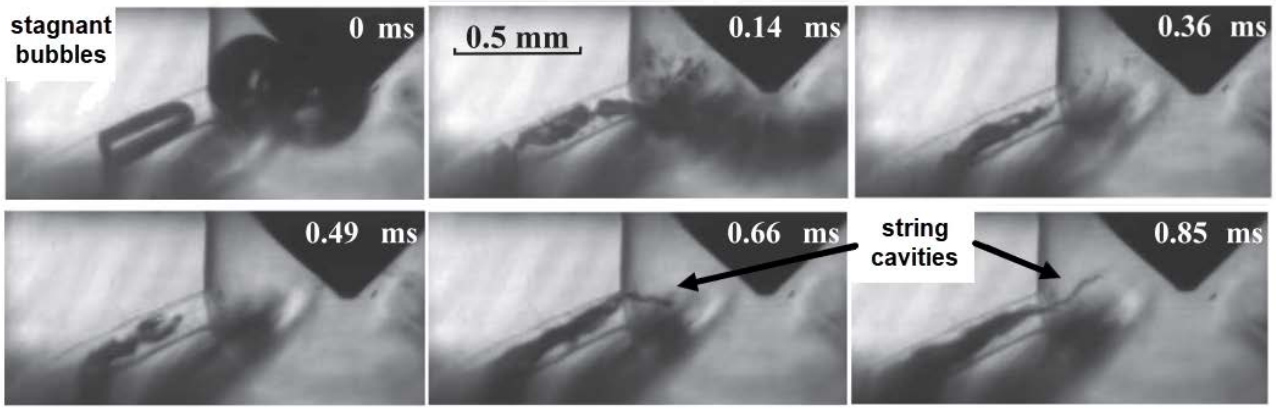

Figure 2. Sequence of representative time instances of an injection event having a duration of 3.5 ms at 300 bars injection pressure. The injection hole diameter is 0.160 mm[9].

Suitable post-processing and averaging of a large number of time-resolved data can provide useful information on the extent and dynamical behaviour of fuel vapour within the injector during the entire injection event. Figure 3 presents mean vapour (or two-phase mixture) presence probability images corresponding to the high-speed images presented in Figure 2, as produced by a series of different injection events. Also depicted in Figure 3 are the respective standard deviation images, which are suitable for highlighting the transient flow features. The mean images corresponding to the needle-opening phase of the injector operation illustrate that the vapour-presence probability is close to 1 in the lower part of the injection hole, hence denoting the presence cavitation during the needle-valve opening. As also revealed by the standard deviation images, transient features within the injector-nozzle are associated with unstable spray behaviour. The time instances depicted in Figure 3 clearly demonstrate that the upper part of the injected spray plume exhibits a flapping behaviour and the spray cone angle fluctuates.

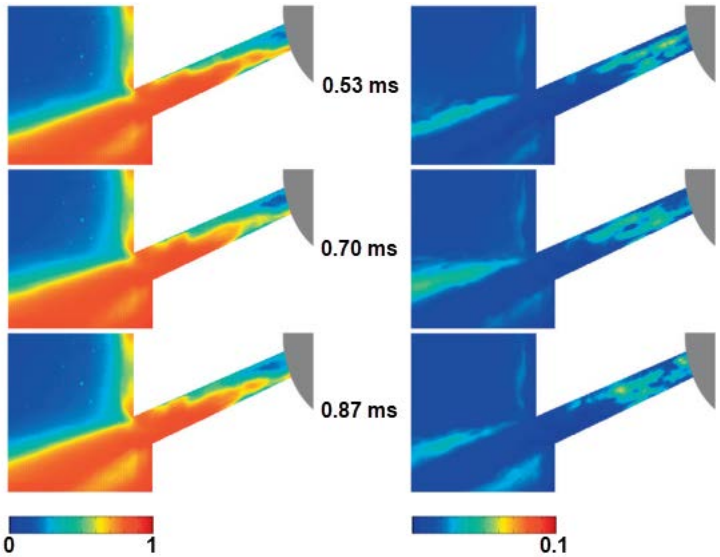

Figure 3. Spatial distribution of average and standard deviation demonstrating the presence of an interphase, i.e cavitation bubbles and two-phase spray mixture inside and downstream of the nozzle exit, respectively during selected time-steps of one injection event corresponding to the raw images depicted in Figure 2[9].

Apart from real-size optical injector tips, fully transparent enlarged injector replicas have been used in experimental investigations allowing cavitating structures to be visualised at larger length-scales, hence enhancing the visualisation resolution[10]. A representative example of an enlarged replica of a 5-hole asymmetrical injector is depicted in Figure 4, with a nominal injection-hole diameter of 1.5 mm[11,12]. The schematic of the arrangement, shown in Figure 4a, incorporates a hollow

slide-type needle that covers the injection holes directly, and minimises the sac volume when fully closed. The injector replica discharges the working medium directly into ambient air under atmospheric pressure and at room temperature and enables the concurrent visualization of the atomization process and the transient cavitating strings arising in the injector-holes and sac regions, as shown in Figure 4b.

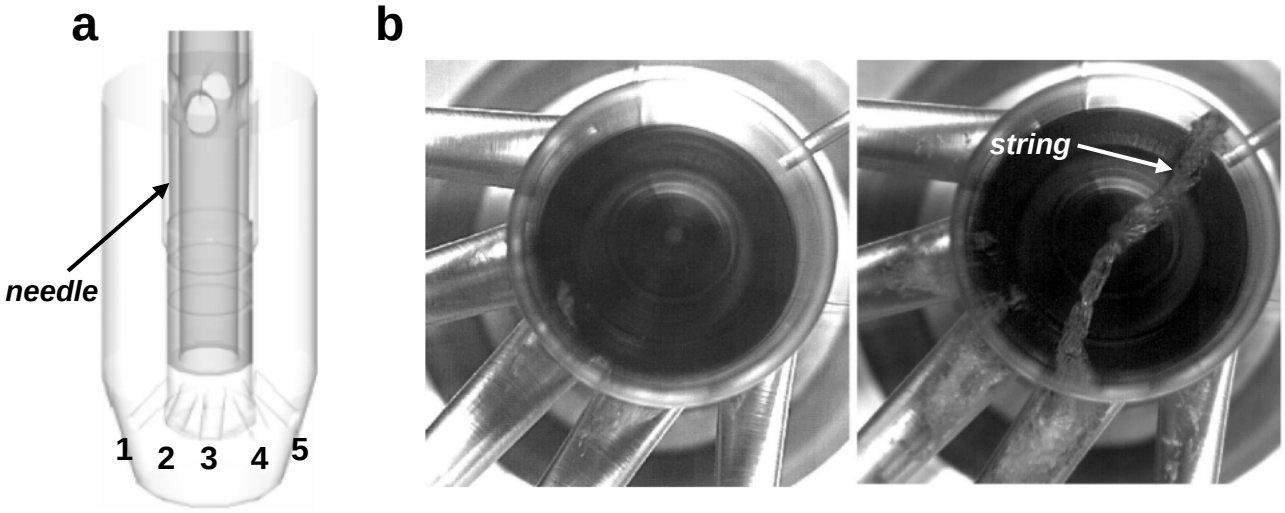

Figure 4. (a) Schematic and bottom-view photograph of the enlarged injector replica, depicting the needle, sac-region an injector holes. (b) Bottom view of the two-phase flow emerging inside the replica. The presence of a string cavity can be clearly discerned in the sac region, also extending into one of the injection holes (CN = 4.0, Re = 68,000)[11,12].

Even more simplified, enlarged single-orifice layouts have been designed and examined with reference to injector flows, in order to shed light to the physical flow processes influencing the onset, development and collapse of cavitation. An injector-mimicking orifice that excludes flow perturbations due to the presence of multiple nozzle holes and transient needle motion is depicted in Figure 5[13]. The optical part comprises an off-set injection hole preceded by an axisymmetric cylindrical flow-path replicating the sac region (Figure 5a). An asymmetric metallic needle, also depicted in Figure 5a, is placed at a fixed, yet adjustable position in the sac region and along with the offset injector nozzle give rise to a flow pattern which leads to the formation of cavitation mainly on one side of the nozzle. Hence, fundamental flow processes associated with cavitation dynamics can be visualised from different angles and in a fully controllable manner by adjusting the position of the metallic needle, as well as the upstream and downstream pressures. A metallic manifold is assembled upstream the examined nozzle configuration, so as to ensure a parallel and unperturbed flow entering the injector-replicating layout. The diesel fuel exiting the nozzle is subsequently discharged into a chamber filled with liquid as well, shown on the lower part of Figure 5c. Hence, the overall configuration can be characterised as a submerged orifice.

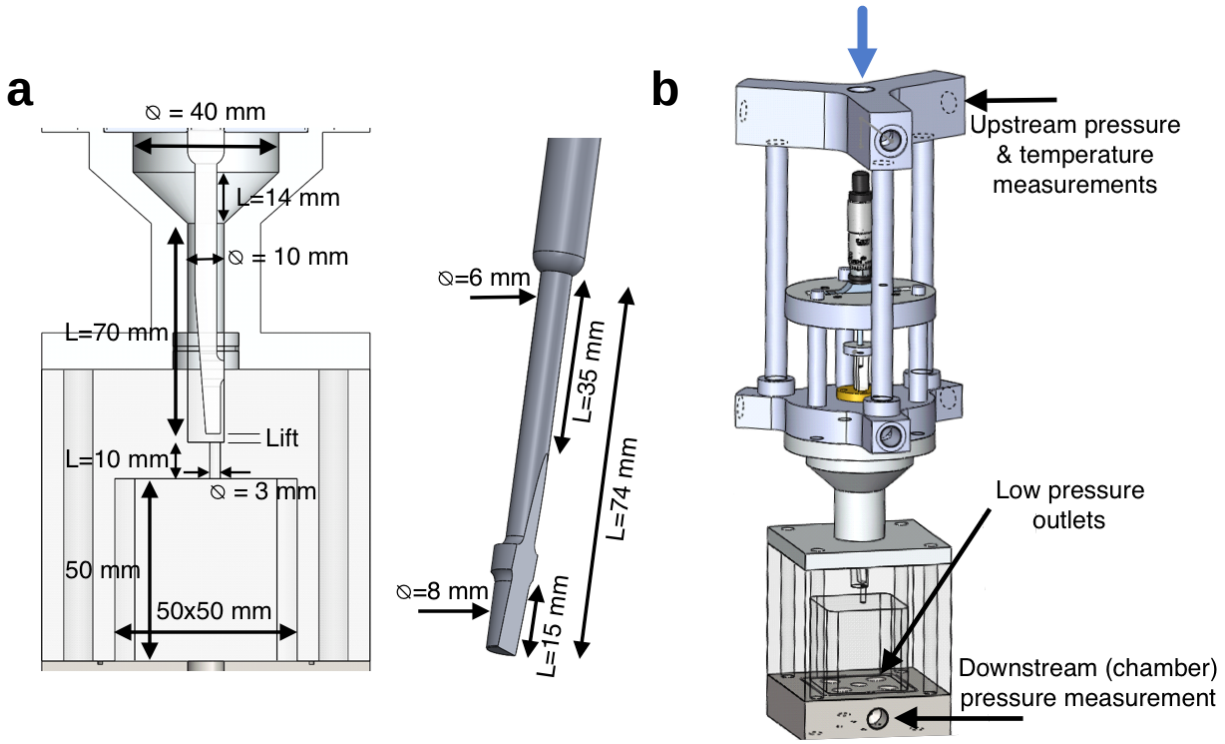

Figure 5. (a) Cross-sectional view of the optical part realizing the single orifice of the injector replica. The metallic needle is also discernible in the middle of the part, while a detailed view of the needle geometry is shown on the right part of the figure. (b) Schematic of the part/manifold assembly[13].

The cavitating flow arising inside the single orifice injector depicted in Figure 5 is elucidated by the sequence of high-speed images presented in Figure 6. For flow conditions characterised by Re=53760 and CN=1.3, a cloud cavity is established in the entrance region of the orifice with an unstable trailing edge from which coherent vortical structures are shed, as highlighted by the red circle in time instances after 0.06ms. The underlying cause for the formation of cloud cavitation in the vicinity of the nozzle wall is the flow separation downstream the geometrical constriction between the needle and needle seat. Hence, the low pressure prevailing in the core of the recirculation pattern leads to the formation of an adverse pressure gradient in the lower part of the nozzle entrance region. This pressure gradient urges liquid to flow opposite to the main flow, as denoted in the detailed view of the 0.04ms time instance (Figure 6). This is a well-known flow mechanism, commonly termed as re-entrant jet in the literature [14,15], which has been demonstrated to be responsible for a cavity shedding sequence, made evident in the specific case as well, by the time instances between 0.04-0.16ms. A coherent vaporous structure can be seen to completely detach from the main cloud at t=0.06ms and being convected towards the nozzle outlet by the main flow in the subsequent time instances. As shown by the time instance at t=0.12ms, the vortical cavitating structure obtains a hairpin shape and eventually collapses once it encounters a flow region of elevated pressure. The vortex ligaments are separated almost entirely at t = 0.16 ms due to viscous decay, while it is worth pointing out that the cavitating vortex collapses in the near-wall region, highlighting a typical mechanism of erosion formation in fuel injectors, as will be discussed in more detail in a subsequent paragraph.

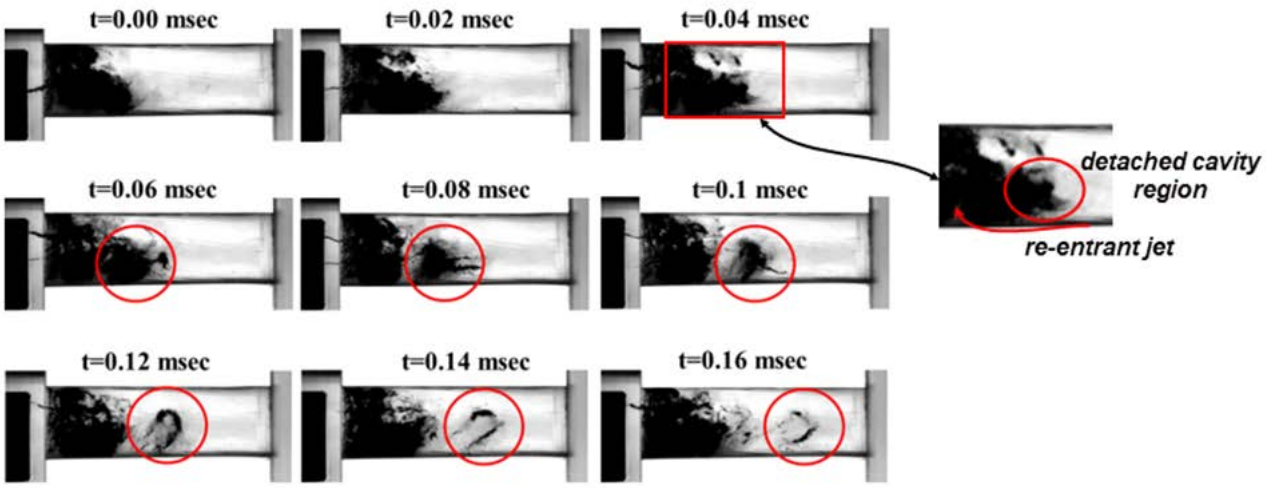

Figure 6. Sequence of side-view high-speed images produced by diffuse back-illumination for the single-orifice replica (needle lift fixed at 0.5mm, CN = 1.3 and Re = 53760)[13]. Flow is from left to right.

Apart from physical inspection of the in-nozzle cavitation development and collapse, statistical treatment of a large number of high-speed images can provide information on the extent of vapour formation and highlight transient features of cavitation owed solely to the flow conditions. Figure 7a presents characteristic time instances of the cavitating flow arising in a similar single-orifice layout as the one depicted in Figure 5, with the exception that the needle tip and sac wall have a hemispherical rather than a flat outline. A cloud cavity, once again sets in at the lower part of the nozzle wall with the distinct feature of exhibiting an oscillating behaviour with a frequency of approximately 296 Hz. Although the cavity-trailing region is unstable, the shedding sequence is associated with a full collapse of a part of the main cloud and hence cannot be attributed to the re-entrant jet mechanism. A mechanism based on the formation of a shock-wave within the separated cloud cavity causing its partial collapse, as described in[16], seems suitable to describe the cavitation dynamics in the specific case. The mean vapour presence probability and standard deviation images depicted in Figure 7b-c clearly highlight the transient behaviour of the cavity development. As can be seen by comparison of the mean images, increase of CN leads to a more extensive cavity attached to the lower part of the orifice wall. Furthermore, it can be deduced through the standard deviation images that increase of CN enhances the oscillatory motion of the cavity, as the extent of the region exhibiting high values increases as well. An additional observation, is that the mean and standard deviation images also highlight the presence of vortical (or string) cavities emanating from the needle tip. Their highly transient nature is once again verified by the low mean and high standard deviation values.

The experimental investigations incorporating the simplified single-orifice injectors discussed above demonstrate that fundamental cavitation processes can be elucidated in such configurations, which omit additional perturbations probable to set in due to geometry complexity. The cavitation regimes identified in enlarged replicas also arise during the operating cycle of actual fuel injectors and therefore identification of the underlying flow processes, e.g. pressure gradients in the orifice, presence and topology of vortical motion, shockwave dynamics, can be directly connected to spray atomisation, injector fuel delivery effectiveness and durability.

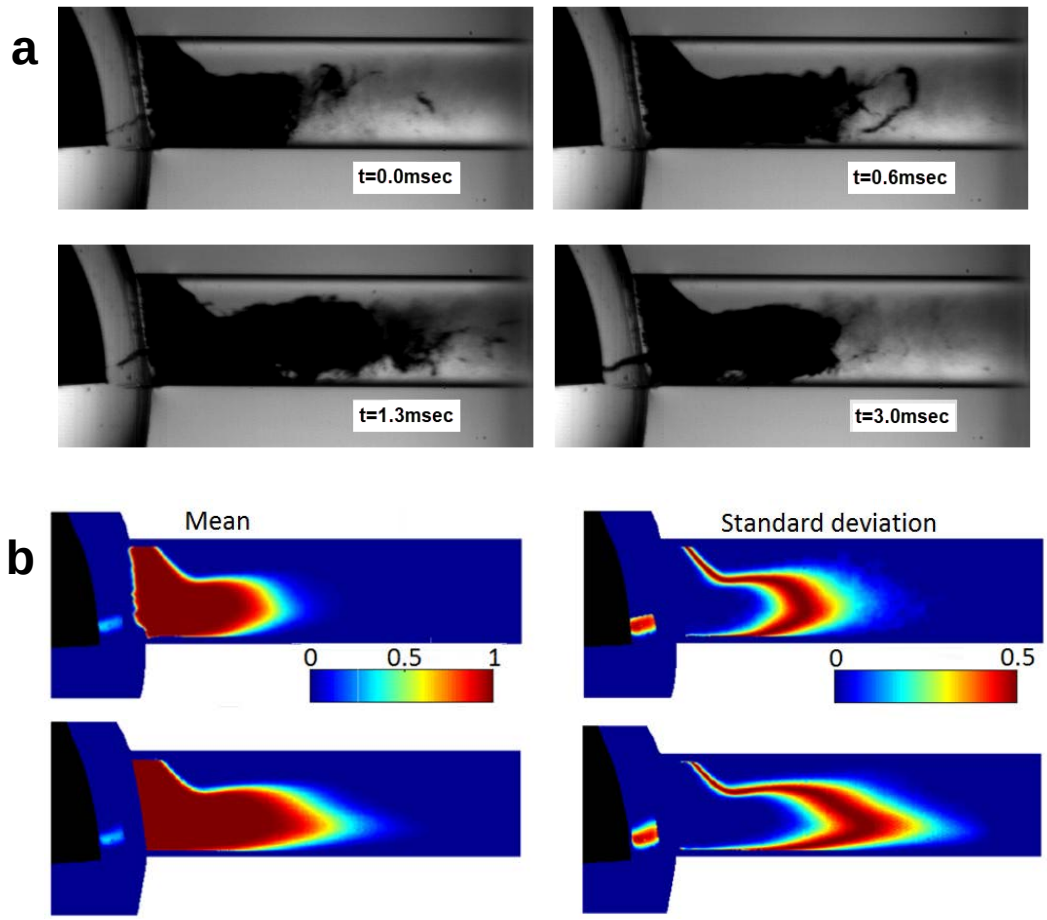

Figure 7. (a) Time instances of the cavitating flow arising in a single-orifice replica with curved needle tip and sac wall. (b) Mean and standard deviation images of the in-nozzle vapour extent (CN=1.6 (top) - 1.8 (bottom), Re=30000 and needle lift of 0.5mm).

X-ray Phase Contrast Imaging (XPCI)

Vapour extent and flow dynamics

Optical imaging, although offers useful information on in-nozzle cavitation characteristics, is limited as a flow visualisation technique by the excessive light scattering in the presence of very low amounts of vapour. In fact, it has been demonstrated that vapour volume fractions of order of 0.15 can completely block a visible light source[16]. XPCI is also based on the interaction of irradiation with matter in the same manner as optical visualisation. A refraction index n can be defined for x-ray beams in the form $n = \delta+\beta i$, with the real part δ and the imaginary part β corresponding to the phase shift intensity and decrease (absorption) of the x-ray wave, respectively[17]. XPCI takes advantage of the δ value of the refractive index corresponding to beam scattering, which is orders of magnitude weaker compared to visible light for hydrocarbon fuel[18]. Contrast fluctuations in a phase-contrast image are therefore designated by much stronger index gradients compared to optical methods and the scattered beam collected by the sensor bears information for all interactions occurring along its path[19]. In other words, features of the cavitating flow, especially in the core of a nozzle, where light visualisation is not possible due to high optical thickness, can be elucidated through XPCI.

An XPCI investigation of the two-phase flow arising in the single-hole injector orifice shown in Figure 7 has been conducted employing a high-flux, 12 keV parallel x-ray beam, as described in detail in[20]. As depicted in Figure 8, the white x-ray beam, after irradiating the injector orifice, is converted to visible light by a scintillator crystal and subsequently captured by a high-speed camera. A sample raw image of the irradiated geometry is shown on the left part of Figure 8 illustrating the beam circular cross-section. Therefore, the orifice is irradiated in a successive manner along its

length, which is divided into five characteristic locations. A spatial overlap has been maintained in all locations, so as to ensure a high signal to noise ratio.

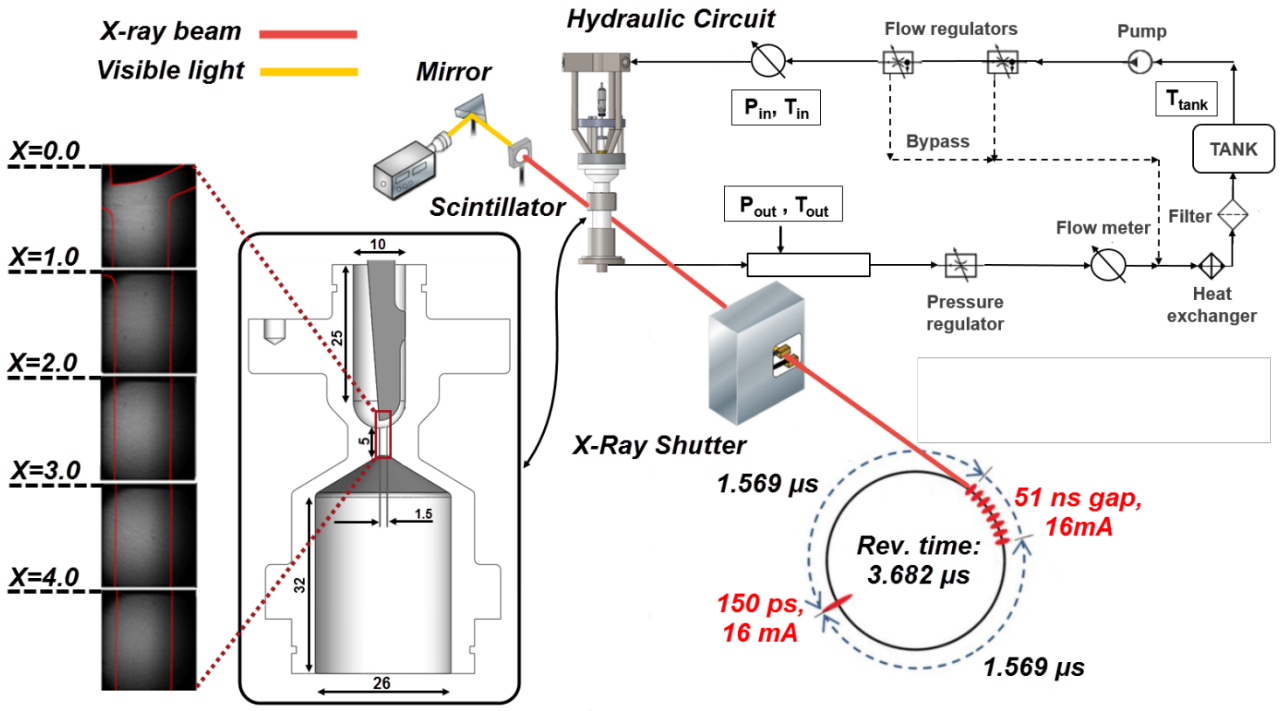

Figure 8. XPCI test rig employing synchrotron radiation. The synchrotron beam-pulsation mode comprises a single pulse of 150 ps in duration, followed by eight short pulses separated by time intervals of 51 ns. Six of the eight pulses of the bunch was utilised allowing a shutter exposure time of 347ns. The spatial resolution in the irradiated characteristic locations (X=0-5mm) of the orifice is 5μm/pixel. The axisymmetric orifice shown was fabricated by a carbon-fibre composite, which causes lower x-ray absorption compared to metals[20].

An indicative post-processed x-ray image is depicted in Figure 9a illustrating the prevailing cavitation regime within the orifice for a needle lift of 0.5mm. Since the cavitation number value characterising the flow conditions is rather high (CN=7.7), the entire orifice length is occupied by a pair of well-established strings with highly unstable interfaces. Attached cavities can also be discerned in the locations closer to the orifice entrance (X=0.0-1.0mm), while it should be noted that the two cavitation regimes can be clearly differentiated in the phase contrast image. A side-view raw image obtained by backlight illumination is also presented as an inset in Figure 9a. Juxtaposition of the two images highlights that interfacial perturbations in the cavity outline, not discernible in the visible-light image, are clearly captured in the x-ray image. Besides, the large extent of cavitation within the orifice blocks light completely and, thus no specific structures can be differentiated in the optical image.

Phase contrast images can be further utilised to extract temporal information regarding the in-nozzle cavitation development. For instance, Figure 9b depicts the mean and standard-deviation images of the vapour extent within the orifice, verifying that, for the specific flow conditions, stable string cavities establish in the largest part of the orifice. It is evident by the close-to-unity probability values obtained that vapour occupies almost the entire orifice cross-section for $X \geq 2.0$, whereas the low standard deviation values in the core of the vaporous structures denote that the strings, although present substantial interfacial fluctuations, their coherence is never disrupted during the manifestation of the phenomenon.

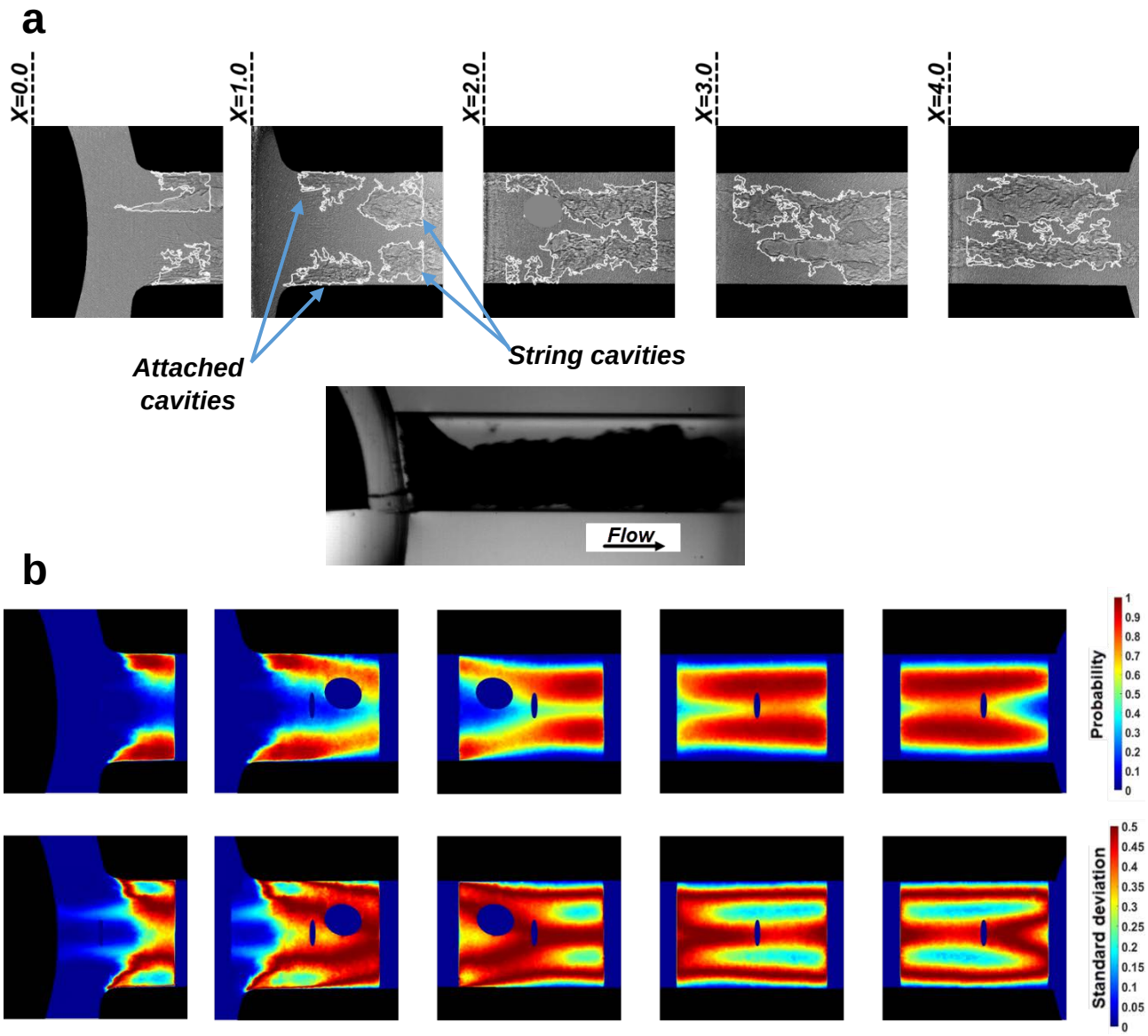

Figure 9. (a) Indicative post-processed time instance of the cavitation development (visualised at 67200 fps) along the orifice length for Re=35500, CN=7.7 and needle lift of 0.5mm (top view). The cavity interphase is denoted by the white line. Vertical lines at the edges of each panel signify the extent of the region where high signal-to-noise ratio could be obtained. Artefacts due to scintillator crystal imperfections have been omitted in grey colour. The inset of the figure shows a representative image obtained by backlight illumination for similar flow conditions. (b) Mean vapour-presence probability and (c) standard deviation images produced by 16000 radiographies for each characteristic location.

The faithful capture of interfacial fluctuations offered by XPCI can be further exploited to obtain information on the underlying secondary flow motion responsible for the cavities onset. It is well established in the literature that string cavities emanate due to pressures lower than the liquid saturation pressure prevailing in the core of coherent vortices. Hence, the well established strings shown in Figure 9 can be correlated to the presence of longitudinal vortices within the orifice. In fact, inspection of the radiographies has verified that for CN>3.0 the cavity interface oscillates laterally with a frequency that is representative of the intensity of the underlying recirculating motion. Figure 10 depicts the Fast Fourier Transform of the cavity radius waveform at a characteristic location depicted in the inset of the figure. By comparing Figures 10a and b, it can be observed that by increase of the Reynolds and cavitation number, the prevailing oscillation frequency f shifts from 340Hz to 544Hz. Also taking advantage of theoretical models correlating the vortical motion intensity Γ with f[21], for instance $\Gamma \sim f \cdot 4\pi^2 \cdot r_c^2$ (r_c being the cavity radius)[22], quantitative information regarding the increase in intensity of the longitudinal vortices can be derive. For instance, since the cavity has been

measured equal to 0.306 to 0.388mm for the cases corresponding to Figure 10a and b, respectively, the recirculation intensity is calculated to be approximately 2.5 higher in the second case.

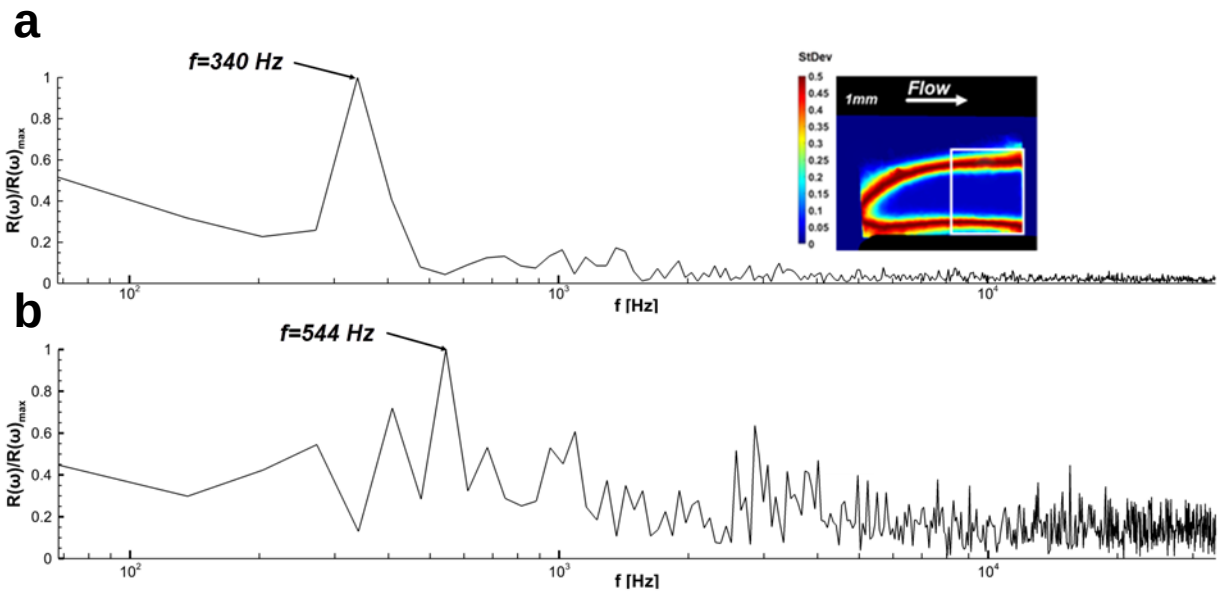

Figure 10. Frequency spectrum of the string cavity radius normalised by the maximum radius recorded: (a) Re=18000, CN =3.2 and (b) Re=35500, CN =4.0 (needle lift of 0.5mm in both cases). Radius values have been averaged along the white-square area of the inset[20].

XPCI, owing to its high temporal and spatial resolution, can also be utilised to obtain quantitative information regarding the dynamics of highly-transient vaporous structure arising for moderately cavitating flows. For instance, referring to the flow layout depicted in Figure 8, Figure 11a, shows the probability of a string cavity to break up into to two (or more). As Re and CN increase, the cavities become more coherent, since the break-up prevailing frequency decreases. Besides, Figure 11b demonstrates that string cavities (an indicative example is shown in the inset of the figure) are expected to live longer prior to their collapse for increased Re and CN. Transient cavitation structures have considerable after-effects regarding injector shot-to-shot fuel delivery variability and induced erosion; hence, identification of their dynamics in a consistent manner is highly valuable for industrial-scale applications, as well.

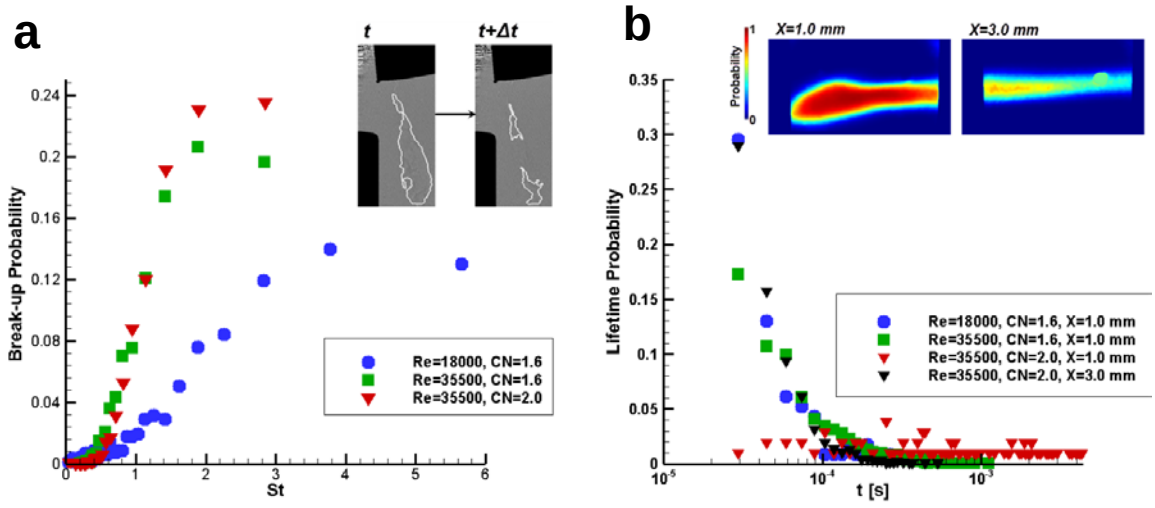

Figure 11. (a) String break-up probability with Strouhal number $St = f \cdot L/U$, f being the break-up frequency, L(=5 mm) the nozzle length and U the nominal flow velocity. (b) String lifetime probability; the inset depicts an indicative structure under consideration[20].

Fuel effects

Fuel additives exhibiting a viscoelastic behaviour added to base Diesel blends in ppm concentrations have been demonstrated to reduce injector deposits but also to have an effect on the topology of the two-phase flow arising in the injector nozzle[23]. XPCI data, although produced through a line of sight method, in essence contain information regarding the 3-dimensional extent of vapour within the orifice and, hence, constitute an ideal method for pinpointing differences between different diesel blends. Figure 12a presents mean vapour-probability images of the flow arising within the single orifice injector (refer to Figure 8) for a base and an additised compound, where viscoelastic polymers have been added in a concentration of 500 ppm w/w. The bulk thermophysical properties of the two compounds are considered to be the same. The contours plots depict a considerably different cavitation topology compared to Figure 9, as cloud cavitation is now prevalent in the major part of the orifice. This different flow behaviour is attributed to the different value of the needle lift, 1.0 mm instead of 0.5 mm, which modifies the recirculation pattern that arises downstream the geometrical constriction. Comparison of the upper and lower panels of Figure 12a makes clear that the presence of additives reduces the extent of cloud cavitation (X≤2.0mm), while on the contrary enhances string cavitation setting in towards the nozzle outlet (X≥2.0mm). The differences in the vapour extent present in the nozzle for the two diesel compounds are quantified by the vapour mean projected area along the orifice length, shown in Figure 12b. The extent of the cloud cavity in the additised diesel case is reduced by approximately 18.5%, whereas the volume occupied by string cavities is increased by about 69% compared to the base diesel fuel. A mechanism for this distinct flow behaviour of viscoelastic diesel fuel, as proposed in[24,25], lies in the interaction of viscoelastic micelles[26] with coherent vortical motion in the macroscale, as well as with turbulence generating vortices in the microscale[27].

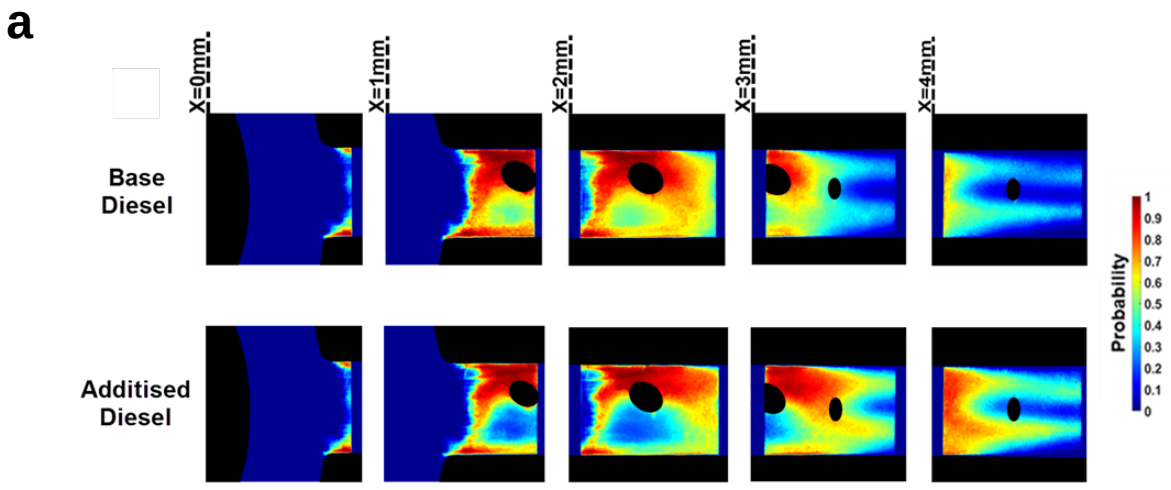

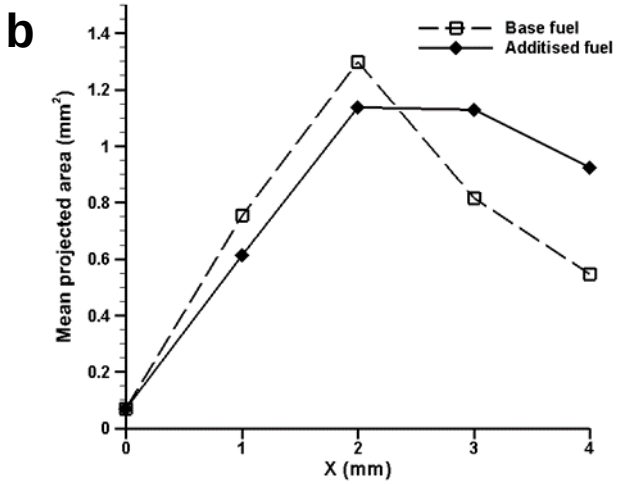

Figure 12. (a) Top-view contour plots of the in-nozzle mean vapour-presence probability for different diesel-fuel compounds. (b) Mean surface of the cavity projection along the orifice length (Needle lift of 1.0 mm, Re=35500, CN=6.0)[25].

Additional information on the effects of viscoelastic additives on string-cavitation dynamics can be obtained with an analysis similar to that presented in Figure 11. Figure 13a comparatively presents the lifetime probability for the two blends of the string cavities arising within the orifice for a needle lift of 0.5; refer to Figure 9 depicting the prevailing cavitation topology for the specific flow conditions. The string lifetime for the additised fuel obtains relatively even probabilities for values up to 0.2ms, whereas the two prevailing frequencies for the base blend are below 0.05 ms. Besides, similar to Figure 10, Figure 13b illustrates the string radius fluctuation in the frequency domain. It is clear that the string fluctuation is more violent regarding the base fuel with at least three prevailing frequencies. On the contrary, only one clear prevailing frequency of 409 Hz is evident for the additised fuel. Once again, the single peak observed and, in fact, at a lower frequency value compared to the base sample, is indicative of a less-perturbed flow. In other words, viscoelastic additives reduce the level of turbulence in the orifice, i.e. the magnitude of the small-scale vortices that would interact and lead to the eventual decay of the string coherence, thus increasing the string lifetime and reducing its interfacial fluctuations. The turbulence-reducing effect of viscoelastic additives has been well documented with reference to single-phase flow[28,29]. Control of cavitation dynamics and, in a second step spray atomisation process in a consistent manner, with the addition of viscoelastic polymers in Diesel fuel is expected to have a tremendous positive impact on the fuel efficiency of diesel engines.

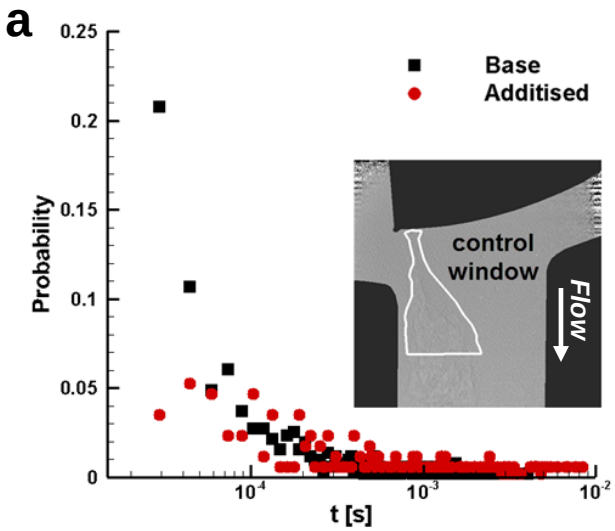

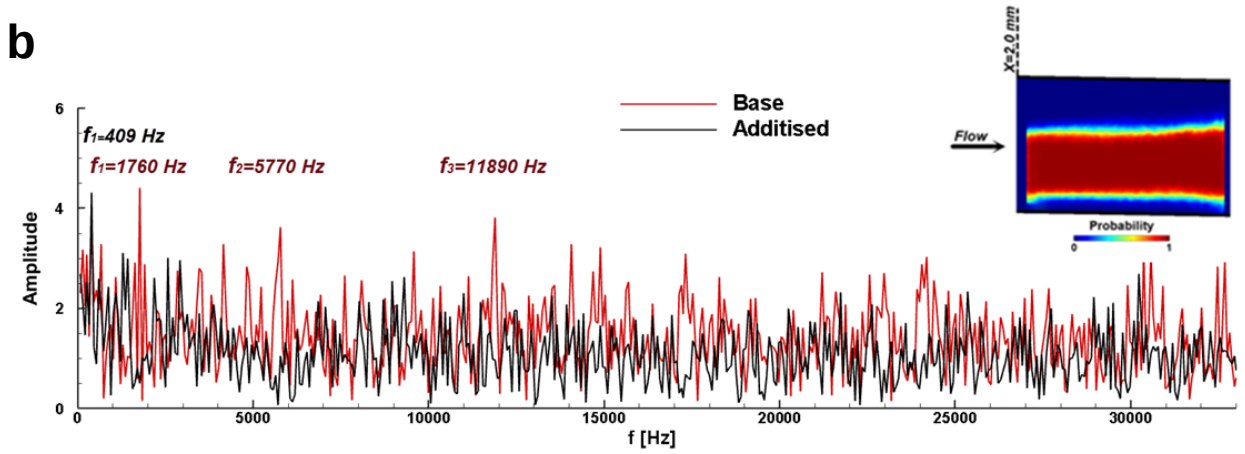

Figure 13. String Cavitation dynamics for needle lift of 0.5mm Re=35500, CN=7.7: (a) String-life probability for the two diesel blends. The control window is located in the vicinity of the needle tip, as denoted by the white line. (b) Fast Fourier Transform of the string radius fluctuation with time.The radius has been averaged in the control winow shown as an inset[24].

Velocimetry employing XPCI

A technique bearing resemblance to Particle Tracking Velocimetry (PTV)[30,31] can be employed in combination with XPCI to provide an estimate of the planar velocity field in the vapour region. The high temporal resolution offered by synchrotron x-ray imaging allows the tracking of distinct flow features, such as vaporous structures or interfacial perturbations, refer indicatively to Figure 14a. Besides, the small exposure time (of the order of nanoseconds) due to the x-ray beam pulsation mode facilitates the accurate capture of the flow fine features without unwanted blurriness. The method enables instantaneous measurements of the local velocity field to be made in regions of the orifice, where the cavitation topology exhibits extensive transient features. As made evident by Figure 14b, point velocity measurements, in both low- and high-CN cases, were made possible in the regions of the flow field exhibiting high vapour presence standard deviation. It has to be emphasised that PTV does not require the addition of seeding particles in the flow that would possibly influence the cavitation formation in the orifice and it is therefore a preferable method for cavitating flows compared to Particle Image Velocimetry (PIV)[32]. Nevertheless, it must also be noted that filtering of a large number of raw radiographies is required to obtain an adequate dataset of point-velocity measurements, since only structures of small size that remain mainly unaltered during consecutive frames are deemed as suitable for velocimetry.

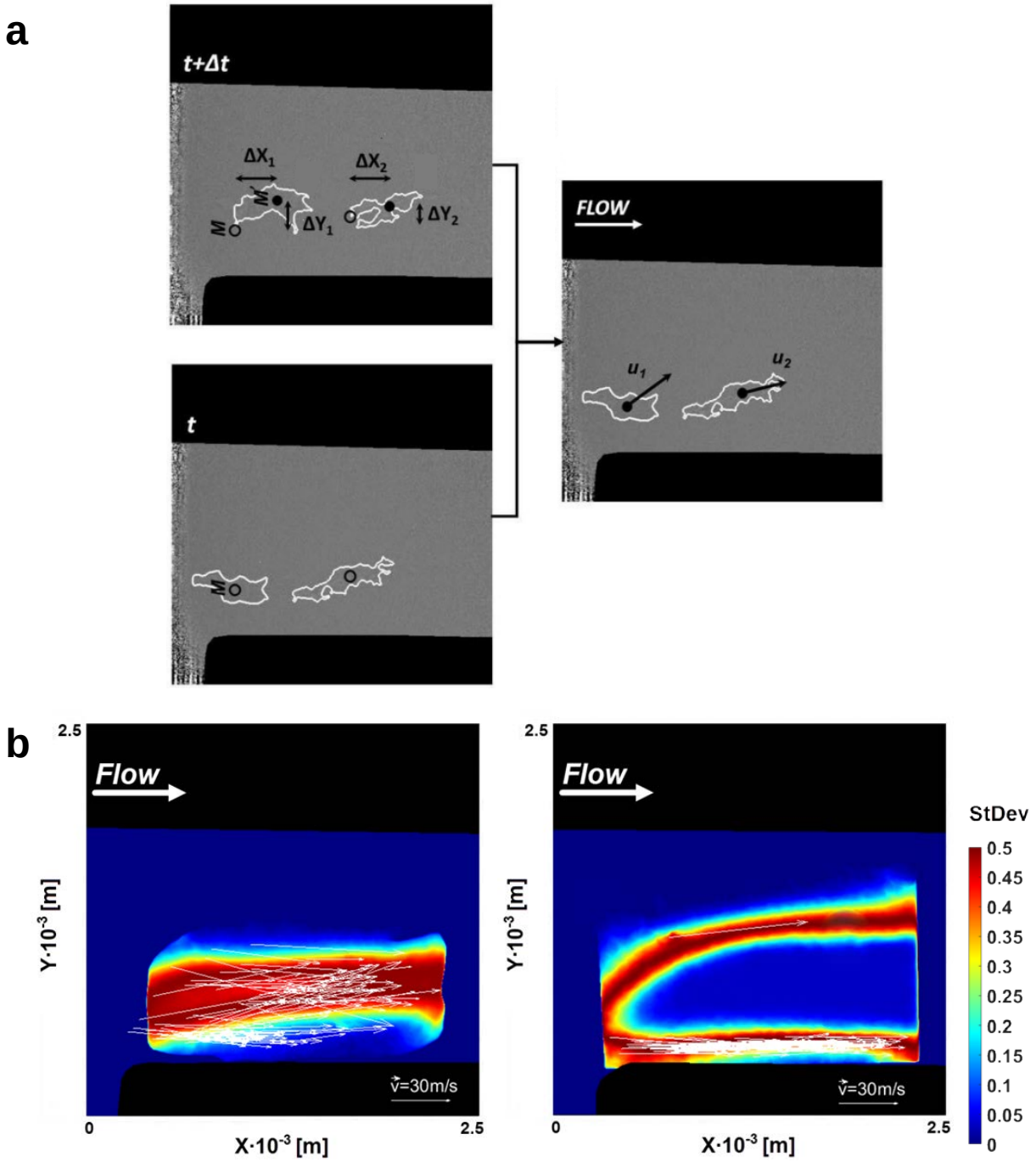

Figure 14 (a) Concept of the PTV method: M and M' is the mass-centre of the identified structure over consecutive frames, with Δt=1/frame-rate (=67890). From the 16000 raw images obtained at each location less than 1% was suitable for velocimetry. The maximum dimension of the structures that have been tracked is less than 700 μm and the mean deviation in their projected area over successive frames is ~8%[20]. (b) Velocity vectors over standard deviation contour plots highlighting indicative locations at which estimates of the local velocity field have been obtained.

An extensive dataset of point-velocity measurements enables the calculation of local planar-velocity fluctuations, indicative of the in-nozzle level of turbulence. Figure 15 illustrates the fluctuations of axial velocity u_0 normalised by the average flow velocity. The average level of turbulence (denoted by the black line) is reduced as *CN* increases, although the Reynolds number increases as well, from 18000 (Figure 15a) to 35500 (Figure 15a). Hence, the presence of coherent, compressible vaporous structures seems to counteract the motion of small-scale vortices and has an overall stabilising effect on the flow field within the nozzle. A similar conclusion regarding the interaction of turbulence and cavitation has been reached through the numerical simulations reported in [33].

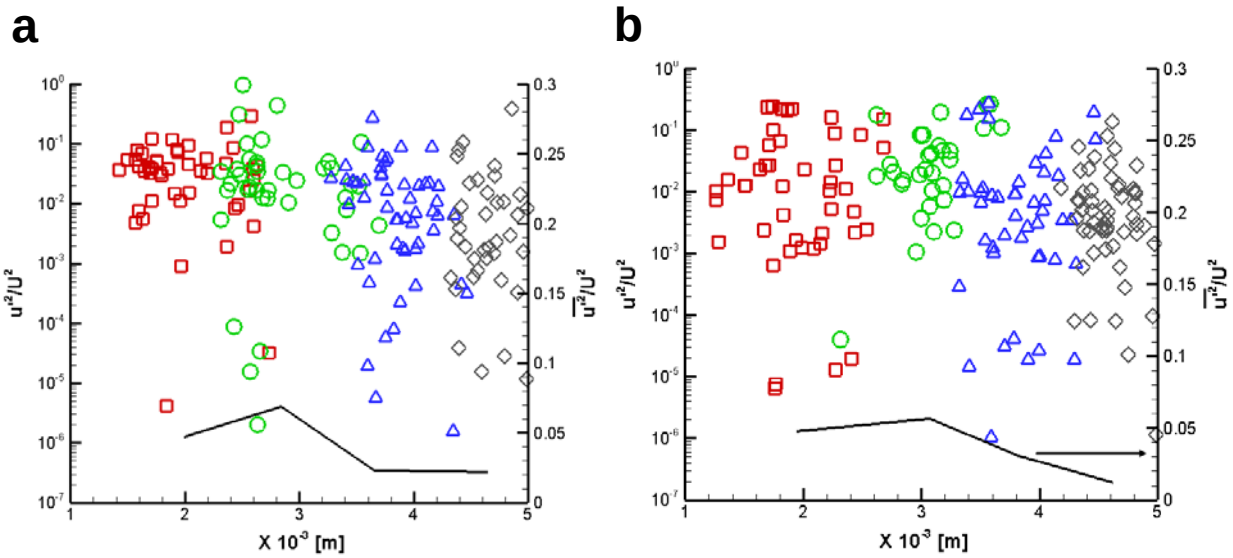

Figure 15 Axial velocity fluctuations (Y ≈0.620±0.04 mm based on the coordinates system shown in Figure 14), (a) Re=18000/CN =3.2, (b) Re=35500/CN =7.7; (□) X=1.0 mm, (○) X=2.0 mm, (Δ) X=3.0 mm, (◊) X=4.0mm[20].

X-ray Computed Tomography (CT) imaging

A shortcoming of optical high-speed imaging is the extensive light-beam scattering due to cavitation presence, which prevents the accurate and volumetric observation of the vaporous structures. Further to that point, the vast majority of optical methods are not capable of correlating the presence of cavitation to the local density of the flow. An alternative to such methods is the utilization of X-ray beams, as has been discussed in the previous paragraphs, which due to their much weaker interaction with matter penetrate the vaporous structures and carry accumulated interaction data through their line of sight. Consequently, their attenuation can be related to the integrated mixture composition along the beam path.

As has been already mentioned in the paragraph discussing XPCI, interaction of an X-ray beam with matter leads to both amplitude decrease and a phase shift of the irradiation wave, as reflected in the complex refractive index through the β and δ coefficients irradiation. Absorption imaging takes advantage especially of the x-ray wave amplitude attenuation and can be employed to derive the vapour mean-path length along the beam line of sight through the Beer-Lambert law[34]:

$$I = I_0 e^{-\mu_l d}$$

where I and I_0 are the attenuated and initial beam intensity, μ_l is the liquid fuel attenuation coefficient and d is the material thickness. Hence, in order to derive the vapour mean path in a cavitating orifice, a normalisation experiment is also required under conditions where cavitation is absent to acquire a reference attenuated beam intensity considering that d is equal to the liquid path length. The characteristic thickness d in an irradiation event of a cavitating flow will be equal to the difference between the liquid and vapour path lengths.

Computed tomography (CT) imaging can be combined with x-ray imaging to collect radiographies of the attenuated x-ray beam from several angles. Reconstruction of the obtained data, referred to as sinograms, can produce a 3D topology image of the irradiated sample. In the case of highly-transient cavitating flows, each projection is acquired over a time scale much larger than the manifestation of the flow phenomena and hence the reconstructed image represents the average vapour topology within the orifice. The first work utilizing X-ray CT for studying cavitation was in an enlarged orifice with a diameter of 1cm, operating with water at pressures of ~0-2bar[35]. The cavitating orifice was examined using a medical scanner, providing volumetric distributions of density inside the orifice. A more recent investigation has been performed at higher pressures (20-40bar) employing an enlarged

injector orifice with internal dimensions identical to the optical part depicted in Figure 5, nevertheless fabricated by a PolyEther-Ether-Ketone (PEEK) plastic polymer[36]. The experiments were conducted at the prototype micro-CT facility available at the University of Bergamo consisting of a 160 kV @ 400 μA open type cone-beam X-ray source[37]. A schematic of the experimental layout comprising the x-ray source, irradiated specimen, scintillator plate and rotary base is illustrated in Figure 16.

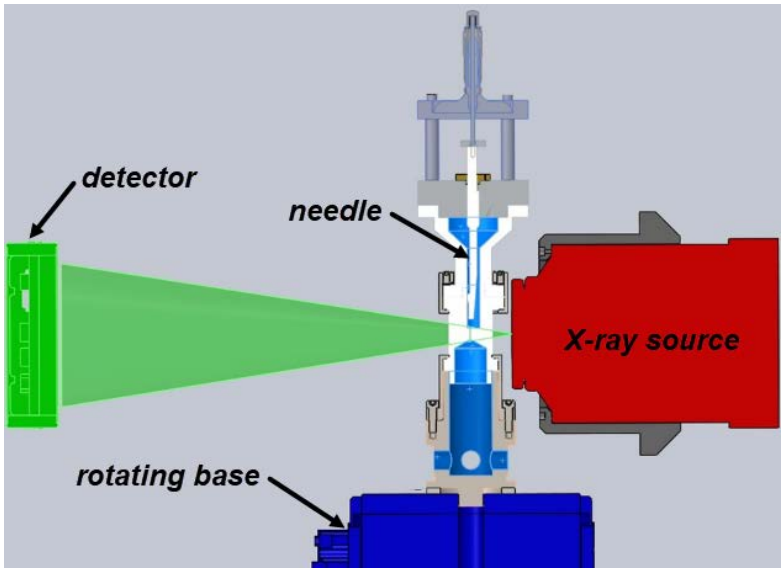

Figure 16 The micro-CT facility employed in [36]**.** Projections were obtained at an angular step 0.6° (600 projections in total), with an acquisition time of 1s per projection.

Figure 17 depicts contours plots of the average liquid fraction for different values of the needle lift. It is evident from the plots at the centre plane of the orifice (left panels of Figure 17a and b) that a lower needle lift (0.5mm instead of 1.0mm) leads to the formation of a more extensive vapour pocket within the orifice, occupying the entire cross section, as illustrated by the front view also shown in Figure 17a. The increased blockage ratio, as the needle lift decreases, leads to a more violent flow separation downstream the constriction, giving rise to a more pronounced cavity. It is interesting to notice in the front view of Figure 17b that a 'halo' of vapour forms at the periphery of the nozzle yet vapour is absent in the upper part of the channel core. This distinctive cavitation behaviour underlines the shortcomings of optical methods, since visible light would be scattered even by this thin film (refer indicatively to Figure 6) thus giving an overestimating impression of the vapour content in the region.

a

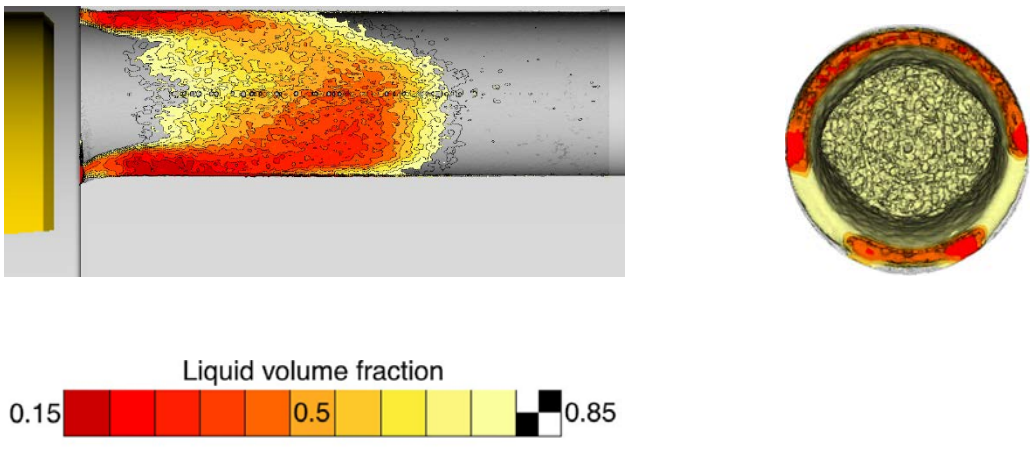

b

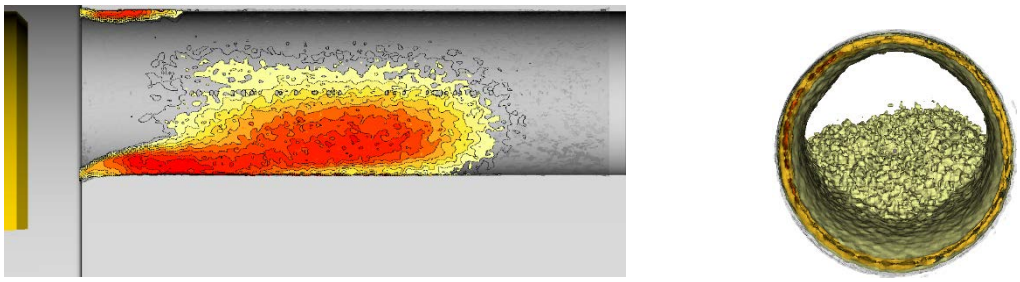

Figure 17 Averaged liquid volume fraction contour plot for CN=2.1: (a) needle lift of 0.5 mm, Re=36500 and (b) needle lift of 1 mm, Re=55500. Left-hand side panels correspond to side-view plots, while right-hand side panels to front-view plots, respectively. Flow is from left to right.

Erosion

A well known property of cavitation is its property to focus energy to small scales. Indeed, whereas large cavities (characteristic size of 1mm) have a potential energy of in the order of ~ 0.1-10mJ, the mechanism of bubble collapse can lead to a concentration of this energy content to sub-micrometer scales, leading to energy density of more than 10kJ/cm^3 enough to cause damage to metals (erosion). The process of erosion development is a complex topic, depending on material properties, such as its yield strength, ultimate strength or fatigue limit, and on flow mechanics aspects. An additional complexity is the temporal scale disparity between flow development, which may have a characteristic time scale of 10^{-3} s and the actual erosion development which can happen in the course of hours.

In general, the process of erosion is considered to be a work-hardening process and to occur in four successive stages. The first stage is the *incubation* stage, during which cavitation collapses introduce plastic deformation to the solid material, without exceeding the ultimate strength, thus there is no material removal. The next stage occurs once the ultimate strength is exceeded and the material can no longer sustain more plastic strain, this material loss occurs; often this happens in an accelerating manner, thus it is termed *acceleration* stage. The next stage is the *steady state* stage where material removal rate remains constant over time and finally removal rate may decrease in the *attenuation* stage. The aforementioned erosion procedure is found in any erosion-prone device; in injectors specifically even the start of material loss is undesired, since it may be associated with:

- strong reduction of performance[38]: alteration of the injector geometry due to erosion may lead to undesired effects on the jet direction and spray characteristics, thus increasing emissions.

- reliability issues: as material is removed from the injector body, stress concentration may occur. This is especially problematic with fuel injectors, as their operating conditions imply very high pressures, potentially leading to catastrophic failure of the injector tip.

The multi-scale nature of cavitation and erosion renders the derivation of cavitation erosion models difficult and there are ongoing efforts for the formulation of generally applicable models. A well accepted scaling law[22] is that mass loss is proportional to the *n*-th power of flow velocity, where *n* is case dependent and varies between 4 - 9. This demonstrates the significance of erosion nuisance in diesel systems, as flow velocity is in the order of several 100m/s. Identified physical mechanisms of erosion can be separated in the following categories[39,40]:

- collapse of a single bubble: at the end of the collapse of a spherical bubble high temperatures and pressures have been detected, resulting to a high intensity pressure wave, with pressures levels of the order of 100MPa.

- microjetting: the existence of pressure gradient around a bubble can lead to an asymmetrical collapse. In that case, part of the bubble collapses faster than the rest of the bubble, forming a characteristic jet with direction opposite to the pressure gradient. This jet may reach velocities up to several 100m/s, producing water hammer pressures in the order of 1000bar.

- collective bubble collapse: the collapse of a bubble within a bubble cloud triggers a cascade of implosions, which tends to enhance the collapse velocities of neighbouring bubbles and to increase the intensity and duration of the resulting pressure wave.

- cavitating vortices: such vortices appear in shear flows and at the rear of attached cavities. Cavitating vortices are considered to be the main cause of severe cavitation erosion in hydraulic machinery. Collapse velocities may be higher than 100m/s and the duration of the stress time is rather long, comparing with the rest mechanisms.

Studies on cavitation erosion span from material science, concerning the resistance of various metals and alloys to cavitation[41], to combined studies coupling fluid dynamic observations with material pitting[42]. In terms of erosion prediction many models rely on energy transfer mechanisms[43], micro-jet formation[44], work-hardening process etc. In more recent works[5,45], erosion has been correlated to the localized flow pressure due to the collapse of cavitation structures and scaling laws have been derived to remove the dependency of collapse events from the numerical resolution.

When considering fuel systems, among the most pioneering works is the systematic investigation of square orifices tested in the Prevero project. In the frame of this project, the cavitation pattern and resulting erosion has been examined in sharp and rounded entrance square orifices operated at pressures of 100-300bar, using diesel-like test oil[46]. The orifices tested were made in a "sandwich" configuration, as a machined metal part placed between two sapphire windows. Depth averaged cavitation probability from high speed imaging and erosion over time were obtained and compared against simulations.

The LES study complemented by an X-ray CT investigation reported by Koukouvinis et al.[33] aimed at the development of validated cavitation models capable of replicating the density distribution and the erosion locations. Indicatively, in Figure 18 the comparison between the experimentally obtained erosion and locations of high pressures from the simulations are shown, demonstrating a good agreement. An important observation of that study was the strong geometrical effects, especially at the orifice entrance, on the cavitating flow.

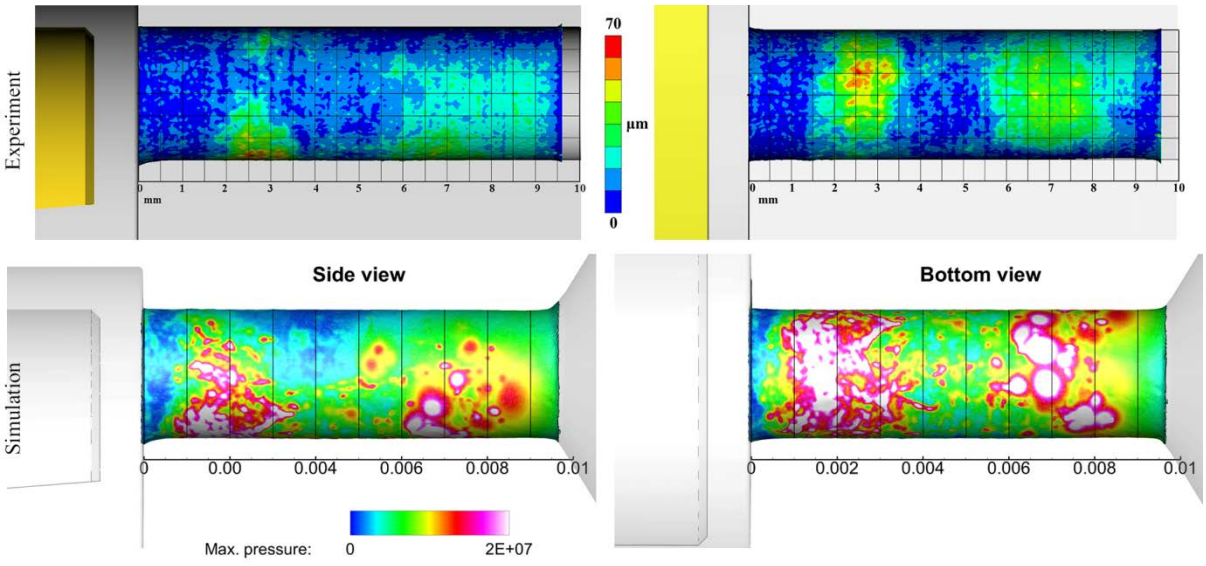

Figure 18. Experimentally observed erosion (top) and numerically obtained locations of high pressures due to cavitation collapse (bottom). Erosion from experiments was obtained by the CT reconstruction of the orifice

wall before and after exposure to cavitation. Progression of erosion is shown after a period of 44hours of operation. The orifice operation was at 55bar (upstream) to 17.4bar (downstream), CN=2.2 and Re=77000. Flow moves from left to right.

Moving towards more realistic configurations, relevant to diesel injectors, among the first works aiming to link cavitation and erosion[47,48] relied on bubble dynamic sub-models relating damage to radiated acoustic pressure. Investigations based on pure Reynolds-Averaged-Navier-Stokes (RANS) turbulence closures performed in the past, showed situational applicability[49,50]. Since then, significant advances have been performed, by employing high resolution, compressibility effects, capable of resolving large cavitation structures and turbulent scales. Notable contributions in the field involve investigations of rectangular orifices during injection to air or liquid[51–53] (an indicative illustration of the flow in such orifices is provided in Figure 19 and Figure 20, derived using computational fluid dynamics and showing the prediction of vortical structures, their interaction with turbulence and the resulting pressure peaks leading to erosion).

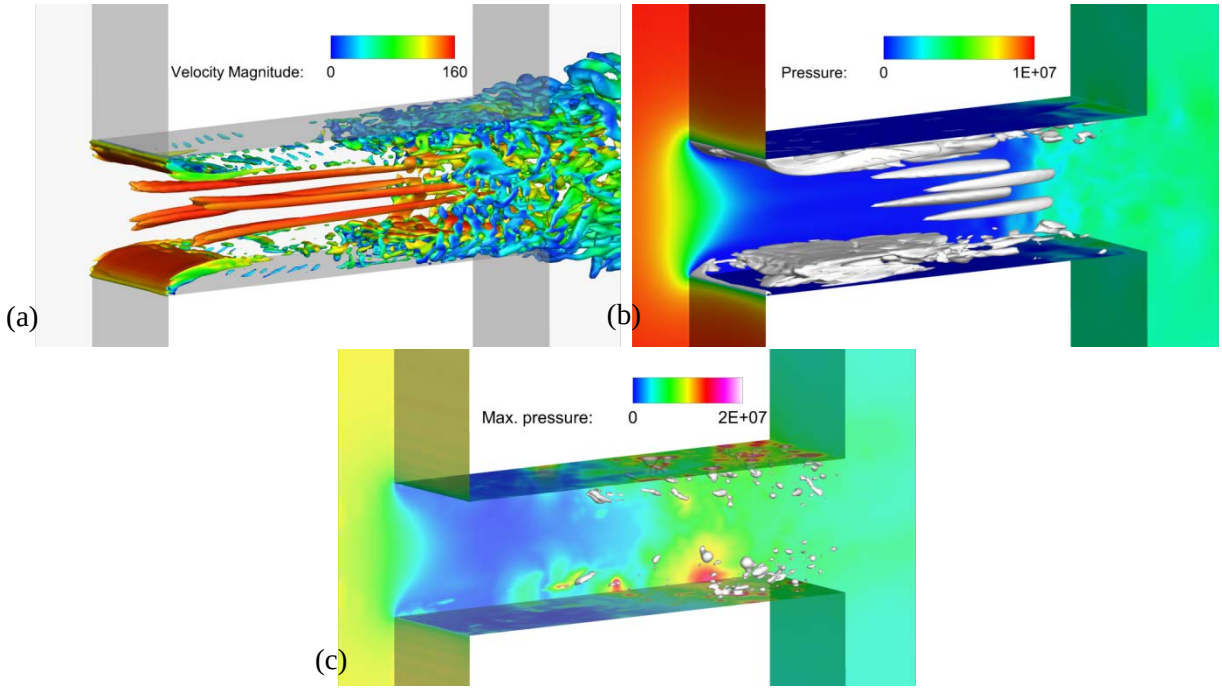

Figure 19. Cavitating flow through a square orifice (cross section 0.3mm x 0.3mm, length 1mm)23, upstream pressure 100bar, downstream pressure 40bar (CN= 1.5, Re= 20000). (a) Instantaneous vortical structures, represented using the *q*-criterion (value 10^{12} $1/s^2$), coloured according to the velocity magnitude; four longitudinal vortex tubes are visible (b) Instantaneous pressure field (background) and cavitation clouds (grey iso-surface vapour volume fraction 50%); note the two cavitation types (attached cavities on the wall and vortex, or string, cavitation at the location of longitudinal vortices). (c) Pressure peaks due to the collapse of vapour structures; local maximum in the order of 1000bar. The flow moves from left to right.

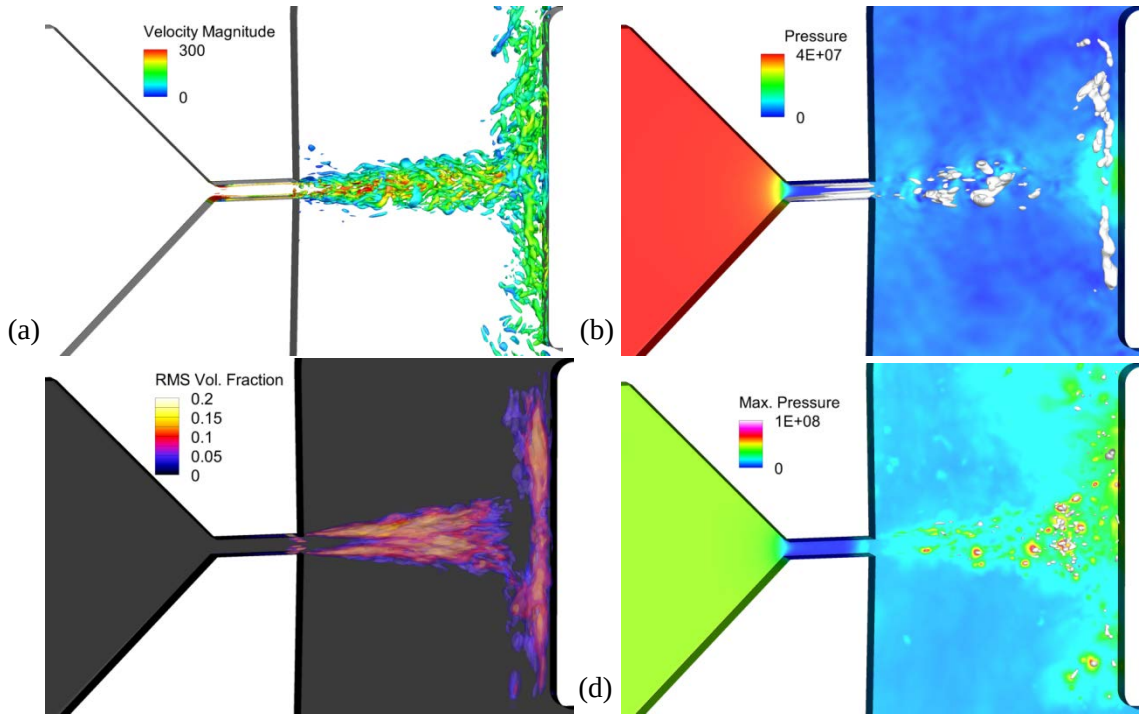

Figure 20. Cavitating flow through a rectangular orifice (cross section: 0.2mm width x 0.3mm depth, length 1mm)[54], under supercavitating conditions; upstream pressure 400bar downstream pressure 24bar (CN= 15.6, Re= 40000). Here a target is placed at 2.95mm from the orifice exit. (a) Instantaneous vortical structures, represented using the *q*-criterion (value 10^{12} $1/s^2$), coloured according to the velocity magnitude; note that within the orifice turbulence is suppressed due to the formation of stable cavities. Strong turbulence develops at the shear layer of the formed jet. (b) Instantaneous pressure field (background) and cavitation clouds (grey iso-surface vapour volume fraction 10%); cavitation at the shear layer is highly transient, (c) root-mean-square of vapour fraction fluctuation; areas of high fluctuations are regions of erosion (d) Pressure peaks due to the collapse of vapour structures; local maximum in the order of 3000bar.

Whereas studying flows in orifices can provide a better understanding of cavitation and erosion mechanisms, the operation of an actual diesel injector is definitely challenging, involving more complicated, moving geometry. Such investigations are limited due to the high complexity and computational cost. Indicatively, the first work[52] to examine computationally diesel injection to air, taking into account compressibility effects, cavitation formation, interaction with non-condensable gas and tracking locations of cavitation collapse required an immense computational cost, with meshes consisting of 35-80million cells. With the current state of computers, such a simulation is prohibitive from an industrial point of view, due to the computational resources and time scales required. Investigations using simpler models[55] exploiting symmetry planes thus reducing the mesh count and computational cost have also been performed. While such models indeed have inherent limitations in terms of describing turbulence or capturing eccentric needle motion, are more tractable from an industrial perspective and have shown good replication of erosive patterns on affected injector designs (see Figure 21).

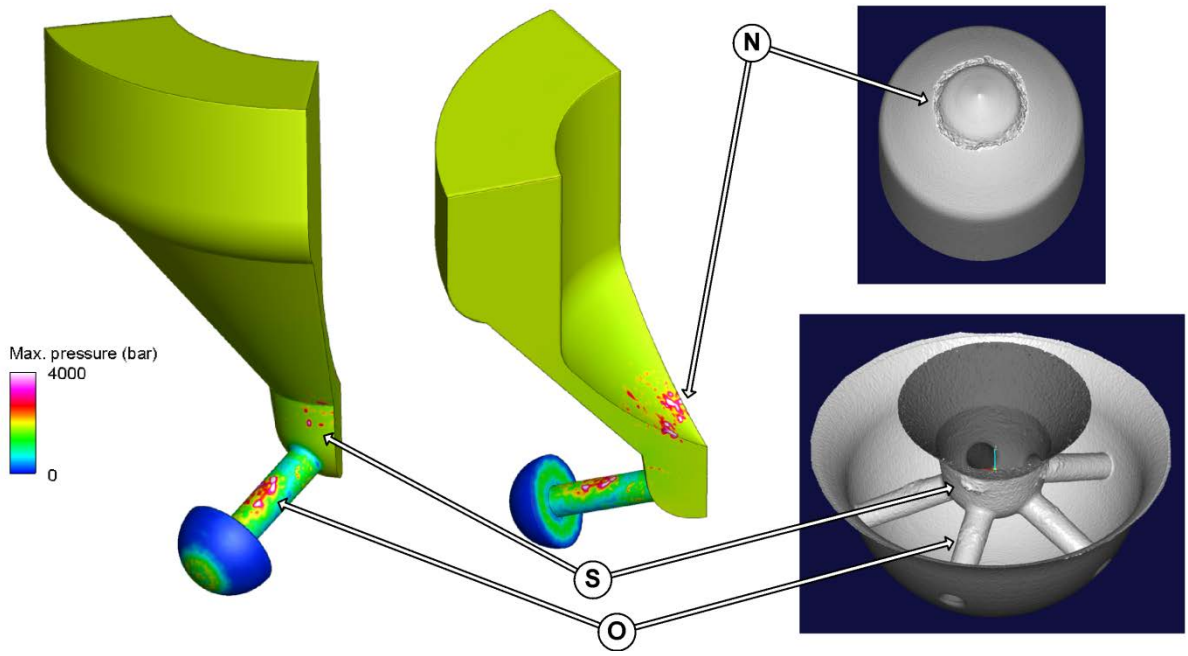

Figure 21. Left: maximum pressures from cavitation collapse on the surfaces of a diesel injector obtained from simulation[55]; note that in the simulation only 1/5th of the complete injector is simulated. Right: Indicative erosion patterns obtained from X-ray tomography of diesel injector. The letters in the cycles correspond to "O" for "orifice", "S" for "Sac" and "N" for "needle". The injector operates at a pressure difference of 1800bar upstream and 50bar downstream (CN~35 and maximum Re~90000).

The aforementioned discussion indicates that cavitation erosion effects can be predicted using numerical models. Erosion locations can be determined by tracking locations of cavitation collapse; moreover their erosive potential can be evaluated in terms of the emitted pressure magnitude. Whereas that magnitude itself is resolution dependent, scaling laws can be defined to predict actual material loss, though calibration is required. In general, erosion prediction necessitates refined models such as scale resolving simulations, which are inherently transient, though the computational cost is still tractable from an industrial perspective.

Real-fluid thermodynamic effects

An additional complexity especially relevant to modern engine operation is the large variations of pressures/temperatures that the fuel undergoes. Inarguably, the most extreme variations appear in modern diesel engines; the fuel may undergo pressure variations from effectively 0bar in cavitating regions up to 2750bar in the common rail[56], and temperatures variations from ambient, 298K, up to 1000K when exposed to the hot gases inside the cylinder. These variations imply considerable changes in the properties of diesel fuel, such as density and viscosity; indicatively dynamic viscosity may change up to 86% and density up to 15%[57], see Figure 22.

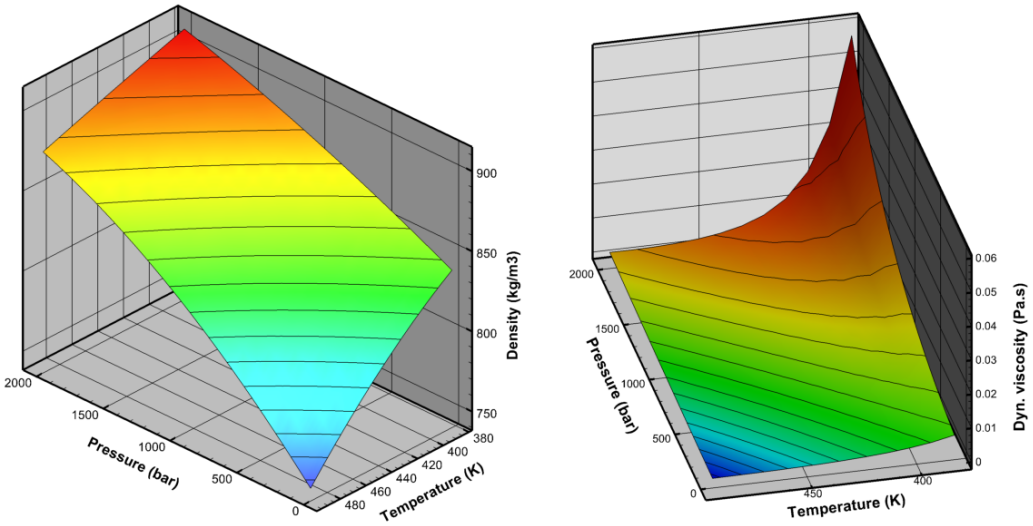

Figure 22. Diesel property variation based on published data[57]; density and dynamic viscosity for a range of pressures and temperatures.

Variation of properties poses additional challenges in the understanding of fuel systems. A notable effect is the temperature change induced by pressure changes. For incompressible fluids it is known that an ideal, adiabatic (isentropic) process implies constant temperature[58]. This statement does not hold for real fluids, where pressure affects density and other thermodynamic properties. Indeed, ideal pressurization of a real-liquid in a diesel fuel pump can result to heating up to 20-30K and fuel expansion during injection can result to localized temperature drop up to 50K, depending on the discharge coefficient[59], see Figure 23. Similar effects appear in gasoline injection equipment as well, but are less pronounced due to lower pressure ratios in comparison to diesel systems.

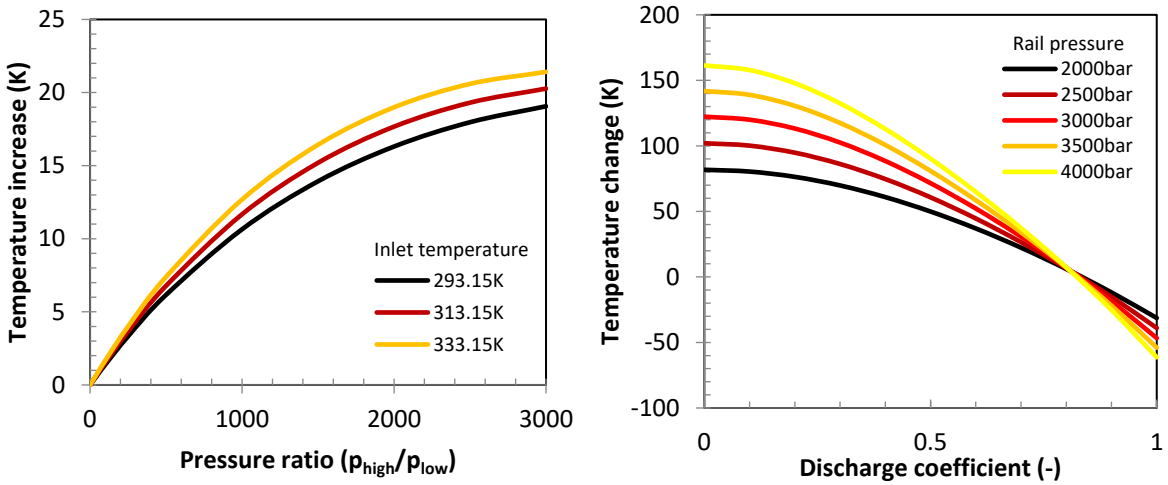

Figure 23. (a) Temperature increase during isentropic diesel fuel compression in pump, for different pump inlet temperatures. Note that the temperature increase applies for ideal compression; actual, non-ideal compression will result to higher temperature increase. (b) Temperature change during fuel passage through a diesel injector, varying the discharge coefficient, c_d, assuming initial fuel temperature of 373K and downstream pressure of 50bar. Derivation of thermodynamic properties is based on published data[57].

It must be highlighted that fuel properties are not easy to define and measure, given the fact that fuels are blends of many different components. Also, fuel composition varies depending on the crude oil source and refinery processing. Hence, there has been increasing effort in measuring properties of fuel components and defining surrogates and models that can approximate the behaviour of actual fuels[60]. For defining adequate models for fuels and fuel components, it is necessary to describe phase

change and transitions around the critical point (see indicatively Figure 24, for dodecane), beyond which there is no distinction between liquid and vapour phases and the latent heat of vaporization is zero.

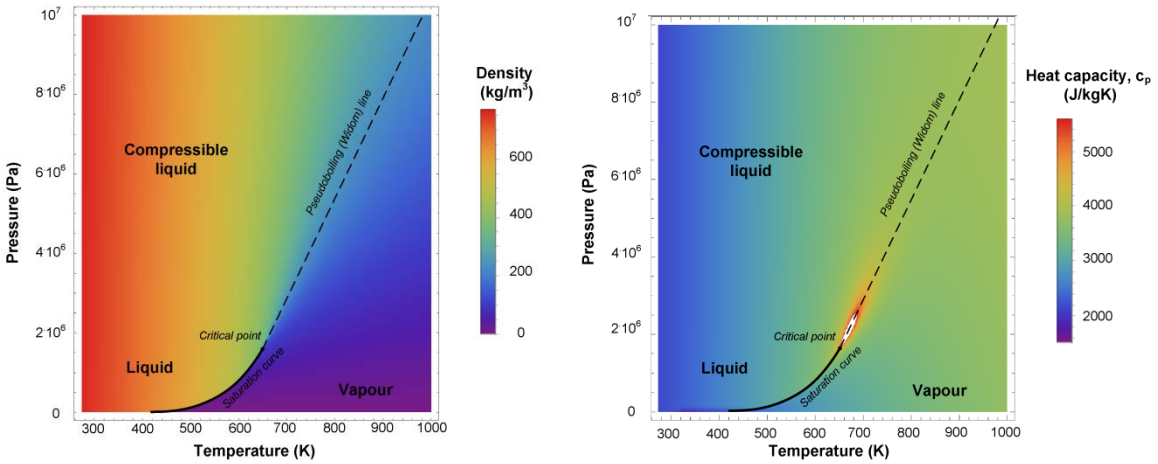

Figure 24. Density (left) and heat capacity (right) variation for different p-T conditions for dodecane, according to NIST Refprop[61]. Note the sharp transition of density along the saturation curve, the smooth variation of density beyond the critical point and the anomalies of heat capacity near the critical point.

Traditionally, models that are capable of describing such phenomena are cubic Equations of State (EoS), with perhaps the earliest example being the Van-der-Waals EoS[58]. Nowadays this formulation has been superseded by more accurate variants, such as the Peng-Robinson or the Redlich-Kwong EoS[58], which can give an overall good representation of thermodynamic property variation, with minimum input (practically three parameters, critical temperature, critical pressure and acentric factor). A common shortcoming of such cubic models is the under-prediction of saturated liquid density and the over-prediction of liquid speed of sound. This deficiency of classical cubic EoS models can have an impact on the accurate prediction of mass flow rate for given pressure difference through an injector[62]. The recent years improvements have been made, capable of much more accurate predictions in relation to traditional cubic models, such as the generalized cubic EoS[63] and Perturbed Chain Statistical Association Fluid Theory (PC-SAFT)[64] model, however these advanced models have not been explored yet widely in studies. Especially the PC-SAFT model is capable of describing the behaviour of mixtures with input based on the molecular structure of the components and their interaction parameters, to provide detailed and accurate predictions of thermodynamic and transport properties.

When moving towards the critical point, the mixing of fuel and surrounding gas departs from the classical atomization. At conditions below the critical point (subcritical) there is a clear distinction of liquid and gaseous phases and surface tension effects are observable[65]. As temperature and pressure conditions move towards, or beyond, the critical point, surface tension effects diminish and there is no longer a clear interface between liquid and gas; instead turbulent mixing prevails (see Figure 25 and Figure 26). Such effects are especially relevant to diesel injection[66]; this can be understood when considering the critical point properties of common hydrocarbons (see Table I), that are components of gasoline and diesel. The trend indicates that as the number of carbon atoms increase in the hydrocarbon molecule, the critical temperature increases and the critical pressure decreases. Considering that gasoline injection happens at relatively low pressure and temperature conditions, the operation regime is more towards classical atomization at subcritical conditions. On the other hand, diesel injection occurs at much higher cylinder conditions, at pressures/temperatures well above the critical point of diesel fuel components.

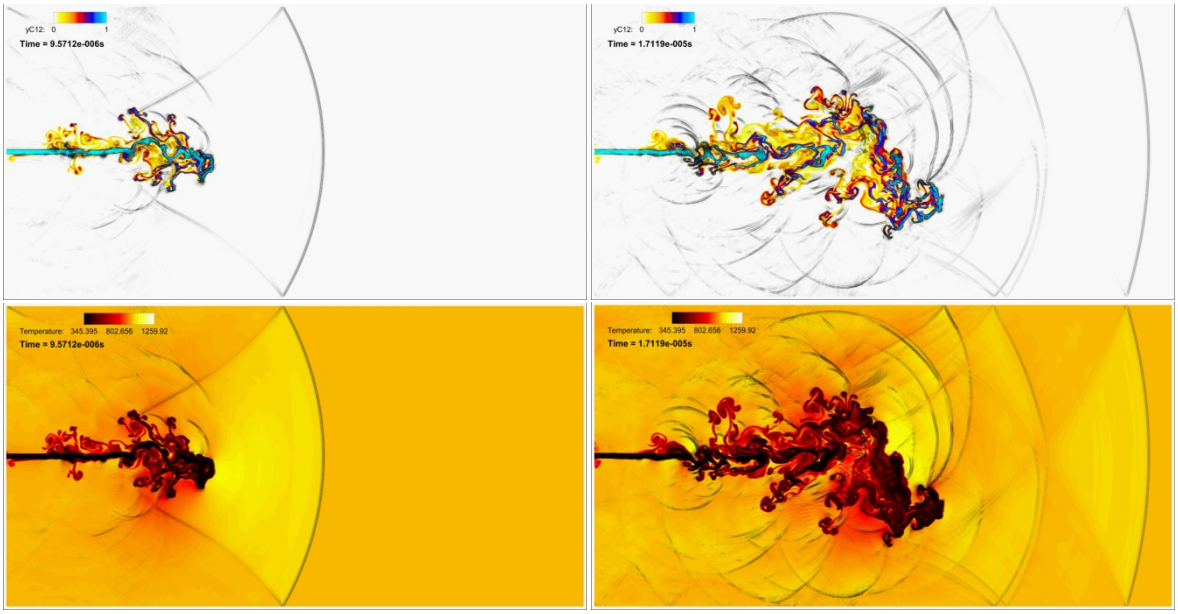

Figure 25. Planar jet of dodecane (363K, 600m/s) to nitrogen (900K, 60bar); the jet has a width of 100μm. Properties based on NIST Refprop[61]. Top row shows mass fraction of dodecane, bottom row shows the temperature distribution. Black shades indicate the formed shock waves from the jet interaction with the stagnant air.

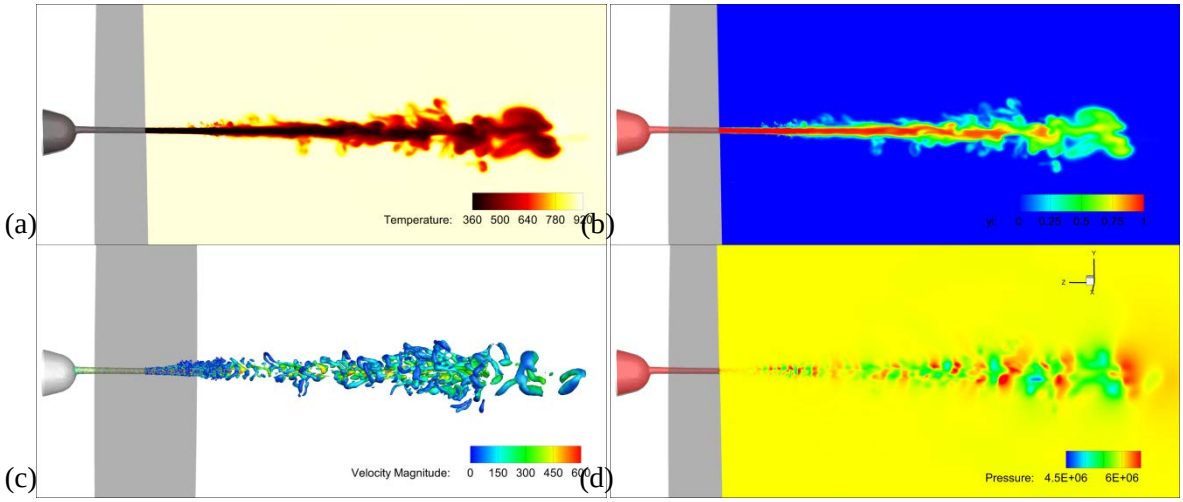

Figure 26. Start-up of ECN Spray-A (non-reacting) configuration; dodecane injection to nitrogen (900K, 60bar). Injection mass flow rate based on the online tool available from ECN (http://www.cmt.upv.es/ECN03.aspx) for injection pressure of 1500bar. Geometry based on published stereolithography (STL) surface. (a) temperature field (b) mass fraction of dodecane (c) pressure field, scaled to min/max. at the external of the injector (d) turbulent structures (q-criterion value 10^{12} s^{-2}), coloured according to velocity magnitude. Time 30μs. Properties based on NIST Refprop[61].

Table I. Critical point properties for indicative fuel/fuel-surrogate components[67].

	Components	T_c (K)	P_c (bar)
Gasoline	Hexane	507.82	30.34
	Heptane	540.13	27.36
	Iso-octane	544	25.72
Diesel	Dodecane	658.1	18.17
	Hexadecane	722.1	14.799
	Docosane	792.2	11.74

It is highlighted that the aforementioned discussion is a rough approximation, given that it is only applicable to single, pure components. Indeed, mixing of different components, such as diesel and nitrogen, alters the critical conditions of the mixture, so that liquid and vapour can exist even if local pressure/temperature conditions exceed the critical conditions of the pure components involved in the mixing. Figure 27 illustrates this effect, showing the pressure-composition lines of nitrogen/dodecane at different temperatures.

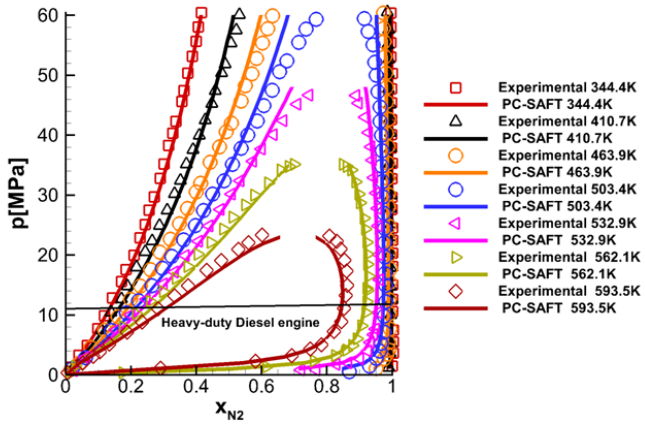

Figure 27. Liquid/vapour saturation lines for different molar compositions of nitrogen/dodecane mixture; comparison between experiments[68] and PC-SAFT model predictions[69]; note that the mixture critical pressure is well above the critical pressure of the individual pure components.

Apart from the complex thermodynamic effects taking place, the flow of fuel and its interaction with gases in the cylinder, also poses complexities. The progressive break-up of fuel to smaller scales, finally vaporizing and mixing with the surrounding air, termed as atomization[70], is a multi-scale process, strongly affected by turbulence and surface tension. Different levels of approximation are commonly employed depending on the level of accuracy and the computational cost that can be afforded, ranging from interface capturing[71] (Volume of Fluid or Level-Set) in primary atomization and Eulerian-Eulerian[72] or Eulerian-Lagrangian[73] models for secondary atomization, or dense-fluid[74] spray models for supercritical/transcritical regimes.

Conclusion

The aforementioned discussion aims to provide a brief overview of multiphase flow phenomena that occur in modern fuel injection systems, with main emphasis in Diesel applications, since those pose the most extreme conditions. Indeed, despite their relative small scale compared to more traditional applications of fluid dynamics (e.g. external aerodynamics), a wealth of phenomena appear combining complex aspects of physics of fluids, such as turbulence, phase transition/vaporization and interfacial flows.

Concerning experimental methods, perhaps one of the most promising and recent developments is the investigation of flow using X-rays. The use of X-rays allows to avoid common drawbacks of optical method, such as optical scattering at fluid interfaces. Further developments of the method involve temporally resolved densitometry, which can provide quantitative information on transient multiphase flows.

Concerning computational techniques, the advancement of computing power has allowed to incorporation of more elaborate and detailed information to be captured in multiphase, cavitating flows, or flows of sprays and fuel jets, offering unprecedented resolution of turbulence and interfacial dynamics. Unfortunately, the computational cost of such investigations is quite prohibitive from a

general perspective, requiring thousands CPU-hours of computing power and often necessitating High Performance Computing (HPC).

References

1. Mitra, P. *et al.* Identification and Characterization of Steady Spray Conditions in Convergent, Single-Hole Diesel Injectors. *SAE Tech. Pap. Ser.* **1**, 1–17 (2019).
2. Reid, B. A., Hargrave, G. K., Garner, C. P. & Wigley, G. An investigation of string cavitation in a true-scale fuel injector flow geometry at high pressure. *Phys. Fluids* **22**, 1–3 (2010).
3. Reid, B. a. *et al.* On the formation of string cavitation inside fuel injectors. *Exp. Fluids* **55**, 1–8 (2014).
4. Gavaises, M., Andriotis, A., Papoulias, D., Mitroglou, N. & Theodorakakos, A. Characterization of string cavitation in large-scale Diesel nozzles with tapered holes. *Phys. Fluids* **21**, 052107 (2009).
5. Schmidt, S. J., Mihatsch, M. S., Thalhamer, M. & Adams, N. A. Assessment of Erosion Sensitive Areas via Compressible Simulation of Unsteady Cavitating Flows. in *Advanced Experimental and Numerical Techniques for Cavitation Erosion Prediction* (eds. Kim, K.-H., Chahine, G., Franc, J.-P. & Karimi, A.) 329–344 (Springer Netherlands, 2014). doi:10.1007/978-94-017-8539-6_14
6. Pickett, L. M., Kook, S. & Williams, T. C. Visualization of Diesel Spray Penetration, Cool-Flame, Ignition, High-Temperature Combustion, and Soot Formation Using High-Speed Imaging. *SAE Int. J. Engines* **2**, 439–459 (2009).
7. Bardi, M. *et al.* Engine Combustion Network: Comparison of Spray Development, Vaporization, and Combustion in Different Combustion Vessels. *At. Sprays* **22**, 807–842 (2013).
8. Westlye, F. R. *et al.* Diffuse back-illumination setup for high temporally resolved extinction imaging. *Appl. Opt.* **56**, 5028 (2017).
9. Mitroglou, N., McLorn, M., Gavaises, M., Soteriou, C. & Winterbourne, M. Instantaneous and ensemble average cavitation structures in Diesel micro-channel flow orifices. *Fuel* **116**, 736–742 (2014).
10. Arcoumanis, C., Gavaises, M., Flora, H. & Roth, H. Visualisation of cavitation in diesel engine injectors. *Mec. Ind.* **2**, 375–381 (2001).
11. Andriotis, A., GAVAISES, M. & ARCOUMANIS, C. Vortex flow and cavitation in diesel injector nozzles. *J. Fluid Mech.* **610**, 195–215 (2008).
12. Andriotis, A. & Gavaises, M. Influence of vortex flow and cavitation on near-nozzle diesel spray dispersion angle. *At. Sprays* **19**, 247–261 (2009).
13. Mitroglou, N., Stamboliyski, V., Karathanassis, I. K., Nikas, K. S. & Gavaises, M. Cloud cavitation vortex shedding inside an injector nozzle. *Exp. Therm. Fluid Sci.* **84**, (2017).
14. Gopalan, S. & Katz, J. Flow structure and modeling issues in the closure region of attached cavitation. *Phys. Fluids* **12**, 895 (2000).
15. Stutz, B. & Legoupil, S. X-ray measurements within unsteady cavitation. *Exp. Fluids* **35**, 130–138 (2003).
16. Ganesh, H., Mäkiharju, S. A. & Ceccio, S. L. Bubbly shock propagation as a mechanism for sheet-to-cloud transition of partial cavities. *J. Fluid Mech.* **802**, 37–78 (2016).
17. Russo, P. *Physical Basis of x-Ray Imaging*. *Comprehensive Biomedical Physics* (Elsevier B.V., 2014). doi:10.1016/B978-0-444-53632-7.00201-X
18. Im, K.-S., Cheong, S.-K., Powell, C. F., Lai, M. D. & Wang, J. Unraveling the Geometry Dependence of In-Nozzle Cavitation in High-Pressure Injectors. *Sci. Rep.* **3**, 3–7 (2013).
19. Linne, M. Analysis of X-ray phase contrast imaging in atomizing sprays. *Exp. Fluids* **52**, 1201–1218

(2012).

20. Karathanassis, I. K. *et al.* High-speed visualization of vortical cavitation using synchrotron radiation. *J. Fluid Mech.* **838**, (2018).

21. Arndt, R. E. A. Cavitation in Vortical Flows. *Annu. Rev. Fluid Mech.* **34**, 143–175 (2002).

22. Franc, J.P., Michel, J. . *Fundamentals of Cavitation*. (Kluwer Publishing, 2005).

23. Naseri, H., Koukouvinis, P., Malgarinos, I. & Gavaises, M. On viscoelastic cavitating flows: A numerical study. *Phys. Fluids* **30**, 033102 (2018).

24. Naseri, H. *et al.* Turbulence and Cavitation Suppression by Quaternary Ammonium Salt Additives. *Sci. Rep.* 1–15 (2018). doi:10.1038/s41598-018-25980-x

25. Karathanassis, I. K. *et al.* Illustrating the effect of viscoelastic additives on cavitation and turbulence with X-ray imaging. *Sci. Rep.* **8**, 1–15 (2018).

26. Dreiss, C. A. Wormlike micelles: where do we stand? Recent developments, linear rheology and scattering techniques. *Soft Matter* **3**, 956 (2007).

27. Tsukahara, T., Motozawa, M., Tsurumi, D. & Kawaguchi, Y. PIV and DNS analyses of viscoelastic turbulent flows behind a rectangular orifice. *Int. J. Heat Fluid Flow* **41**, 66–79 (2013).

28. Dimitropoulos, C. D., Sureshkumar, R. & Beris, A. N. Direct numerical simulation of viscoelastic turbulent channel flow exhibiting drag reduction: Effect of the variation of rheological parameters. *J. Nonnewton. Fluid Mech.* **79**, 433–468 (1998).

29. Pereira, A. S., Mompean, G., Thais, L. & Soares, E. J. Transient aspects of drag reducing plane Couette flows. *J. Nonnewton. Fluid Mech.* **241**, 60–69 (2017).

30. Kitagawa, A., Hishida, K. & Kodama, Y. Flow structure of microbubble-laden turbulent channel flow measured by PIV combined with the shadow image technique. *Exp. Fluids* **38**, 466–475 (2005).

31. Sathe, M. J., Thaker, I. H., Strand, T. E. & Joshi, J. B. Advanced PIV/LIF and shadowgraphy system to visualize flow structure in two-phase bubbly flows. *Chem. Eng. Sci.* **65**, 2431–2442 (2010).

32. Mueller, A., Dreyer, M., Andreini, N. & Avellan, F. Draft tube discharge fluctuation during self-sustained pressure surge: Fluorescent particle image velocimetry in two-phase flow. *Exp. Fluids* **54**, (2013).

33. Koukouvinis, P., Mitroglou, N., Gavaises, M., Lorenzi, M. & Santini, M. Quantitative predictions of cavitation presence and erosion-prone locations in a high-pressure cavitation test rig. *J. Fluid Mech.* **819**, 21–57 (2017).

34. Duke, D. J., Kastengren, A. L., Tilocco, F. Z., Swantek, A. B. & Powell, C. F. X-Ray Radiography Measurements of Cavitating Nozzle Flow. *At. Sprays* **23**, 841–860 (2013).

35. Bauer, D., Chaves, H. & Arcoumanis, C. Measurements of void fraction distribution in cavitating pipe flow using x-ray CT. *Meas. Sci. Technol.* **23**, 055302 (2012).

36. Mitroglou, N., Lorenzi, M., Santini, M. & Gavaises, M. Application of X-ray micro-computed tomography on high-speed cavitating diesel fuel flows. *Exp. Fluids* **57**, (2016).

37. Lorenzi, M., Mitroglou, N., Santini, M. & Gavaises, M. Novel experimental technique for 3D investigation of high-speed cavitating diesel fuel flows by X-ray micro computed tomography. *Rev. Sci. Instrum.* **88**, (2017).

38. Som, S., Aggarwal, S. K., El-Hannouny, E. M. & Longman, D. E. Investigation of Nozzle Flow and Cavitation Characteristics in a Diesel Injector. *J. Eng. Gas Turbines Power* **132**, 42802–42812 (2010).

39. van Terwisga, T. J. C., Fitzisimmons, P. A. & Li, Z. R. Cavitation Erosion – A review of Physical Mechanisms and Erosion Risk Models. in *7th International Symposium On Cavitation* (2009).

40. Leighton, T. G. *The acoustic bubble*. (Academic Press , 1994).

41. Franc, J.-P., Riondet, M., Karimi, A. & Chahine, G. L. Material and velocity effects on cavitation erosion pitting. *Wear* **274**–**275**, 248–259 (2012).

42. Petkovšek, M. & Dular, M. Simultaneous observation of cavitation structures and cavitation erosion. *Wear* **300**, 55–64 (2013).

43. Fortes Patella, R., Choffat, T., Reboud, J.-L. & Archer, A. Mass loss simulation in cavitation erosion: Fatigue criterion approach. *Wear* (2013). doi:http://dx.doi.org/10.1016/j.wear.2013.01.118

44. Dular, M. & Coutier-Delgosha, O. Numerical modelling of cavitation erosion. *Int. J. Numer. Methods Fluids* **61**, 1388–1410 (2009).

45. Mihatsch, M. S., Schmidt, S. J. & Adams, N. A. Cavitation erosion prediction based on analysis of flow dynamics and impact load spectra. *Phys. Fluids* **27**, (2015).

46. Skoda, R. *et al.* Numerical simulation of collapse induced shock dynamics for the prediction of the geometry, pressure and temperature impact on the cavitation erosion in micro channels. *WIMRC 3rd International Cavitation Forum 2011* (2011). doi:10.13140/2.1.2676.9287

47. Gavaises, M. Flow in VCO nozzles with cylindrical and tapered holes and link to cavitation erosion and engine exhaust emissions. *Int. J. Engine Res.* **9**, 435–447 (2008).

48. Gavaises, M., Papoulias, D., Andriotis, A., Giannadakis, E. & Theodorakakos, A. Link between cavitation development and erosion damage in Diesel fuel injector nozzles. *SAE World Congress & Exhibition*, (2007).

49. Edelbauer, W., Strucl, J. & Morozov, A. Large Eddy Simulation of cavitating throttle flow: SIMHYDRO 2014. in *Advances in Hydroinformatics, Part III* (eds. Gourbesville, P., Cunge, J. A. & Caignaert, G.) 501–517 (Springer Singapore, 2016). doi:10.1007/978-981-287-615-7_34

50. Koukouvinis, P., Naseri, H. & Gavaises, M. Performance of Turbulence and Cavitation Models in Prediction of Incipient and Developed Cavitation. *Int. J. Engine Res.* (2016).

51. Egerer, C. P., Hickel, S., Schmidt, S. J. & Adams, N. a. Large-eddy simulation of turbulent cavitating flow in a micro channel. *Phys. Fluids* **26**, 085102 (2014).

52. Örley, F., Hickel, S., Schmidt, S. J. & Adams, N. A. Large-Eddy Simulation of turbulent, cavitating fuel flow inside a 9-hole Diesel injector including needle movement. *Int. J. Engine Res.* (2016).

53. Koukouvinis, P. & Gavaises, M. Simulation of throttle flow with two phase and single phase homogenous equilibrium model. *J. Phys. Conf. Ser.* **656**, 12086 (2015).

54. Bauer, W., Iben, U. & Voss, M. Simulation of cavitating flow in injection systems. *Numerical analysis and Simulation in Vehicle Engineering, VDI Berichte* **1846**, (2004).

55. Koukouvinis, P., Gavaises, M., Li, J. & Wang, L. Large Eddy Simulation of Diesel injector including cavitation effects and correlation to erosion damage. *Fuel* **175**, 26–39 (2016).

56. Egler, W. *et al.* Fuel Injection Systems. in *Handbook of Diesel Engines* (eds. Mollenhauer, K. & Tschöke, H.) 127–174 (Springer-Verlag Berlin Heidelberg). doi:10.1007/978-3-540-89083-6

57. Kolev, N. *Multiphase Flow Dynamics 3*. (Springer Berlin Heidelberg, 2007). doi:10.1007/978-3-540-71443-9

58. Borgnakke, C. & Sonntag, R. *Fundamentals of Thermodynamics*. (Wiley, 2008).

59. Strotos, G., Koukouvinis, P., Theodorakakos, A., Gavaises, M. & Bergeles, G. Transient heating effects in high pressure Diesel injector nozzles. *Int. J. Heat Fluid Flow* **51**, 257–267 (2015).

60. Vidal, A., Rodriguez, C., Koukouvinis, P., Gavaises, M. & McHugh, M. A. Modelling of Diesel fuel properties through its surrogates using Perturbed-Chain, Statistical Associating Fluid Theory. *Int. J. Engine Res.* 146808741880171 (2018). doi:10.1177/1468087418801712

61. Lemmon, E. W., Bell, I. H., Huber, M. L. & McLinden, M. O. NIST Standard Reference Database 23:

Reference Fluid Thermodynamic and Transport Properties-REFPROP. *Natl. Inst. Stand. Technol. Stand. Ref. Data Progr.* (2018). doi:10.18434/T4JS3C

62. Matheis, J. & Hickel, S. Multi-component vapor-liquid equilibrium model for LES of high-pressure fuel injection and application to ECN Spray A. *Int. J. Multiph. Flow* **99**, 294–311 (2018).

63. Kim, S.-K., Choi, H.-S. & Kim, Y. Thermodynamic modeling based on a generalized cubic equation of state for kerosene/LOx rocket combustion. *Combust. Flame* **159**, 1351–1365 (2012).

64. Gross, J. & Sadowski, G. Perturbed-Chain SAFT: An Equation of State Based on a Perturbation Theory for Chain Molecules. *Ind. Eng. Chem. Res.* **40**, 1244–1260 (2001).

65. Crua, C., Manin, J. & Pickett, L. M. On the transcritical mixing of fuels at diesel engine conditions. *Fuel* **208**, 535–548 (2017).

66. Dahms, R. N. & Oefelein, J. C. On the transition between two-phase and single-phase interface dynamics in multicomponent fluids at supercritical pressures. *Phys. Fluids* **25**, 92103 (2013).

67. Anitescu, G., Bruno, T. J. & Tavlarides, L. L. Dieseline for Supercritical Injection and Combustion in Compression-Ignition Engines: Volatility, Phase Transitions, Spray/Jet Structure, and Thermal Stability. *Energy & Fuels* **26**, 6247–6258 (2012).

68. García-Córdova, T., Justo-García, D. N., García-Flores, B. E. & García-Sánchez, F. Vapor−Liquid Equilibrium Data for the Nitrogen + Dodecane System at Temperatures from (344 to 593) K and at Pressures up to 60 MPa. *J. Chem. Eng. Data* **56**, 1555–1564 (2011).

69. Rodriguez, C., Vidal, A., Koukouvinis, P., Gavaises, M. & Mchugh, M. A. Simulation of transcritical fluid jets using the PC-SAFT EoS. *J. Comput. Phys.* **374**, 444–468 (2018).

70. Tryggvason, G., Scardovelli, R. & Zaleski, S. *Direct Numerical Simulations of Gas–Liquid Multiphase Flows*. (Cambridge University Press, 2011).

71. Ghiji, M., Goldsworthy, L., Brandner, P. A., Garaniya, V. & Hield, P. Numerical and experimental investigation of early stage diesel sprays. *Fuel* **175**, 274–286 (2016).

72. Vujanović, M., Petranović, Z., Edelbauer, W., Baleta, J. & Duić, N. Numerical modelling of diesel spray using the Eulerian multiphase approach. *Energy Convers. Manag.* **104**, 160–169 (2015).

73. Anez, J. *et al.* Eulerian–Lagrangian spray atomization model coupled with interface capturing method for diesel injectors. *Int. J. Multiph. Flow* **113**, 325–342 (2019).

74. Müller, H., Niedermeier, C. A., Matheis, J., Pfitzner, M. & Hickel, S. Large-eddy simulation of nitrogen injection at trans- and supercritical conditions. *Phys. Fluids* **28**, 15102 (2016).